TU Wien

Master's Thesis

Electrochemical and structural properties of $SrTiO_3$ thin films prepared by a sol-gel process

Author:
Mina Ghorbanzadeh

Supervisors:
Univ.Prof. Dipl.Phys. Dr.rer.nat.
Jürgen Fleig

Univ.Ass. Dipl.-Ing.
Claudia Steinbach

A thesis submitted in fulfillment of the requirements for the degree of
Master of Science at the

Institute of Chemical Technologies and Analytics

Date , Vienna

Mina Ghorbanzadeh

Abstract

Strontium titanate ($SrTiO_3$), commonly referred to as STO, exhibits the perovskite crystal structure and is characterized by the general formula ABO_3, featuring both ionic and covalent bonds. STO is a model material for electronic applications. Deliberate tuning of point defects allows variation of electrochemical properties and thus enables application in a wide range of technologies, such as batteries, fuel cells, and more.

In this study, a sol-gel process was employed to produce thin films of STO, as this method offers a cost-effective alternative to physical vapor deposition, such as pulsed laser deposition (PLD). Titanium tetrabutoxide and strontium acetate hemihydrate were dissolved in 2-methoxyethanol and acetic acid, respectively, and then combined to create a 0.2 M solution. The mixture was stirred for half an hour and aged for 24 hours. Subsequently, STO thin films were deposited on Yttria-stabilized zirconia (YSZ) and Nb-doped $SrTiO_3$ (Nb:STO) substrates using the spin-coating process, followed by a heat treatment for drying and pyrolysis on a hot plate.

The STO thin films were subsequently annealed in an air atmosphere at temperatures ranging from 550 to 850 °C to investigate the crystallization of the perovskite phase. Grazing Incidence X-Ray Diffraction (GIXRD) measurements confirmed that STO thin films exhibit a perovskite structure above 650 °C annealing with a crystal parameter of 3.9 Å, validating the effectiveness of the sol-gel process in reproducing the perovskite structure. Analysis using Laser Ablation Inductively Coupled Plasma Mass Spectrometry (LA-ICP-MS) indicated the presence of Sr vacancies in the STO thin films, as the resulting stoichiometry showed a Sr deficiency between $Sr_{0.8}Ti_1O_3$ and $Sr_{0.95}Ti_1O_3$.

The STO thin film conductivity and defect chemistry at 500 °C was assessed through electrochemical Electrochemical Impedance Spectroscopy (EIS), utilizing a novel sample setup where STO thin films served as the working electrode on YSZ with GDC/Fe_2O_3 counter electrodes, enabling precise control of the oxygen non-stoichiometry through a bias voltage between +1 V and -1 V vs. Fe/FeO, equaling to the wide oxygen partial pressure range of 10^{-3} bar down to 10^{-55} bar. The results indicated a high concentration of oxygen vacancies at low partial pressures. Measurements to even lower $p(O_2)$ were limited only by the increasing electronic conductivity of the YSZ electrolyte, which prevented further voltage application to increase oxygen vacancies concentration in STO.

The electronic conductivity of STO thin films on purely electronic conducting Nb:STO substrates revealed very low conductivity values in air similar to the intrinsic conductivity of undoped STO (= pseudo-intrinsic). Finally, STO thin films were tested as anodes in oxygen-ion batteries, demonstrating the material's potential for such applications.

Kurzfassung

Strontiumtitanat ($SrTiO_3$), allgemein als STO bezeichnet, weist die Perowskitkristallstruktur auf und wird durch die allgemeine Formel ABO_3 charakterisiert, die sowohl ionische als auch kovalente Bindungen aufweist. STO ist ein Modellmaterial für elektronische Anwendungen.

Durch gezielte Abstimmung von Punktdefekten kann eine Variation der elektrochemischen Eigenschaften erreicht werden, was Anwendungen in einer Vielzahl von Technologien wie Batterien, Brennstoffzellen und mehr ermöglicht.

In dieser Studie wurde ein Sol-Gel-Prozess eingesetzt, um Dünnschichten von STO herzustellen, da diese Methode eine kostengünstige Alternative zur physikalischen Gasphasenabscheidung, wie gepulster Laserablation (PLD), darstellt.

Titaniumtetrabutoxid und Strontiumacetathemihydrat wurden jeweils in 2- Methoxyethanol und Essigsäure gelöst und dann kombiniert, um eine 0,2 M Lösung zu erzeugen. Die Mischung wurde eine halbe Stunde gerührt und 24 Stunden gealtert. Anschließend wurden STO-Dünnschichten auf Yttrium stabilized Zirconia (YSZ) und Nb-doped SrTiO3 (Nb:STO) Substraten mittels des Spin-Coating-Prozesses abgeschieden, gefolgt von einer Wärmebehandlung zum Trocknen und Pyrolyse auf einer Heizplatte.

Die STO-Dünnschichten wurden anschließend in Luftatmosphäre bei Temperaturen von 550 bis 850 °C annealed, um die Kristallisation der Perowskitphase zu untersuchen. GIXRD Messungen bestätigten, dass STO-Dünnschichten oberhalb von 650 °C Annealing eine Perowskitstruktur mit einem Kristallparameter von 3,9 Å aufweisen, was die Bildung der Perowskitstruktur bestätigt. Die Analyse mittels LA-ICP-MS ergab das Vorhandensein von Sr- Leerstellen in den STO-Dünnschichten, da die resultierende Stöchiometrie eine Sr-Defizienz zwischen $Sr_{0,8}Ti_1O_3$ und $Sr_{0,95}Ti_1O_3$ zeigte.

Die Leitfähigkeit und Defektchemie der STO-Dünnschicht wurden durch EIS ermittelt, wobei ein neuartiger Probenaufbau verwendet wurde, bei dem STO-Dünnschichten als Arbeitselektrode auf YSZ mit GDC/Fe_2O_3 Gegenelektroden dienten, wodurch eine präzise Kontrolle der Sauerstoff-Nichtstöchiometrie durch eine Bias-Spannung zwischen +1 V und -1 V gegen Fe/FeO ermöglicht wurde, was einem breiten Sauerstoffpartialdruckbereich von 10^{-3} bar bis hinunter zu 10^{-55} bar entspricht. Die Ergebnisse deuteten auf eine hohe Konzentration an Sauerstoffleer-

stellen bei niedrigen Partialdrücken hin. Messungen bis hinunter zu noch niedrigeren p(O_2) wurden nur durch die zunehmende elektronische Leitfähigkeit des YSZ Elektrolyten begrenzt, die eine weitere Spannungserhöhung zur Vergrößerung der Sauerstoffleerstellenkonzentration in STO verhinderte.

Die elektronische Leitfähigkeit von STO-Dünnschichten auf rein elektronisch leitenden Nb:STO-Substraten zeigte in Luft sehr niedrige Leitfähigkeitswerte, die denen der intrinsischen Leitfähigkeit von undotiertem STO entsprachen (= pseudo-intrinsisch). Schließlich wurden STO Dünnschichten als Anoden in Sauerstoffionenbatterien getestet, was das Potenzial des Materials für solche Anwendungen demonstrierte.

Contents

1 Introduction

Strontium titanate ($SrTiO_3$) is extensively studied due to its promising electrochemical and structural properties. STO finds applications in diverse fields, including Dynamic Random-Access Memory (DRAM) [1] and photovoltaic cells (PV) [2, 3]. STO can be synthesized using various methods such as pulsed laser deposition (PLD), aerosol chemical vapor deposition (ASCVD) [4], and sol-gel processes[5–7]. Synthesizing STO thin films via the sol-gel method offers several advantages compared to other deposition methods, including reproducibility, low-temperature production, high purity, and cost-effectiveness.

In this investigation, STO thin films prepared via the sol-gel method were investigated for their potential as oxygen ion batteries. With the urgent need to address global warming and reduce CO_2 emissions, research on harvesting and storing renewable energy is critical for the near future. STO thin films hold promise for energy harvesting as a photovoltaic cell [3] and energy storage material in an oxygen ion battery. This inovatice type of oxygen ion batteries may represents a significant step in energy storage technology. By taking advantage of the power of oxygen ions, this novel approach not only promises high efficiency but also underscores a crucial shift towards sustainable and eco-conscious energy solutions. Through engineering and cutting-edge research, these batteries offer a hope for a future where energy storage is both robust and environmentally responsible [8].

The working principle of oxygen ion batteries is rooted in the chemical potential change of oxygen. Utilizing Mixed Ion Electron Conductors (MIEC), the oxygen stoichiometry can be tuned, making these materials suitable for oxygen ion batteries. This capability enables the conduction of ions and the storage of neutral oxygen within their structure. Oxygen insertion and removal in MIEC occur through oxidation and reduction processes. The potential of the half-cell oxygen ion battery is determined by the reducibility of the material. Ionic defects constitute the majority of defects in such materials, so changing their concentaration changes the chemical potential of the battery. Sealing is required to prevent oxygen uptake from the atmosphere [9].

In comparison to lithium-ion batteries, where lithium ions serve as charge carriers intercalating between the anode and cathode based on chemical potential differences, oxygen ion batteries operate similarly but oxygen is the ion which intercalate in between of anode and cathode. By applying voltage to the anode and reducing the anode material, oxygen vacancies are generated. This electrochemical state can then be stored. Analogous to lithium ion battert, the less reduciale the cation, the more negative is charged anode and larger is the battery voltage. Lithium is the lightest metal with a high chemical potential in the electrochemical series (-3.05 V vs NHE in nats). However, also T^{+4} in STO possesses a high electrochemical potential, which can lead to voltages near 2 V versus 1 bar oxygen. STO exhibits characteristics of MIEC, making it suitable for use as an anode in oxygen ion batteries due to its ability to conduct ions and electronic charge.

2 Theoretical Background

2.1 Structure of strontium titanate

A crystal structure consists of an infinite three-dimensional arrangement of crystalline units, often referred to as unit cells. Each unit cell is composed of an array of atoms, and this overall arrangement can conform to one of the 14 Bravais lattice types discovered by the French mathematician Auguste Bravais in 1850 [10]. Strontium titanate ($SrTiO_{3-\delta}$) belongs to the perovskite crystal structure category, characterized by the general formula ABO_3. In this formulation, A represents a larger cation than B, and their combined valence is +6. Specifically, in the case of $SrTiO_{3-\delta}$, Sr^{+2} occupies the A site, while Ti^{4+} resides in the B site. Perovskite crystal structures, including STO ($SrTiO_3$), exhibit a cubic arrangement at room temperature with space group Pm3m (schematic illustration of the structure shown in fig. 2.1). However, when the temperature is below 105 K, a structural phase transition occurs, resulting in the formation of a tetragonal structure with the I4/mcm symmetry. This shift in crystal symmetry highlights the dynamic behavior of strontium titanate under varying temperature conditions. STO is a semiconductor with an indirect band-gap of ca 3.2 eV, with the lattice constant of 3.9 Å. [11, 12]. Figure 2.1 shows a schematic illustration of the unit cell of STO. Moreover, optical properties of STO can be influenced by impurities or doping.

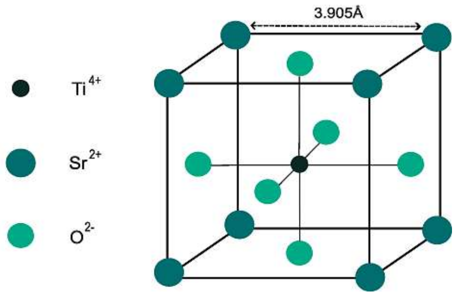

Figure 2.1: The strontium titanate unit cell with lattice constant of 3.9 Å

2.2 Defect chemistry

The differentiation between ideal crystals and non-ideal crystals is referred to as defects. In nanomaterials, particularly in thin films, defects play a crucial role. Due to the high surface energy in these materials, defects are highly prone to occurrence and significantly impact their properties. Crystals usually consist of defects that can manifest in 0, 1, 2, or 3 dimensions. Zero-dimensional defects refer to the atomic scale. One-dimensional, or line defects, involve imperfections in the crystal lattice. Two-dimensional defects are planar, representing irregularities or disruptions in the alignment of atoms or molecules within the crystal lattice. Three-dimensional, or bulk defects, are related to macroscopic issues affecting the volume of the material (for examples, see Table 2.1). Point defects have significant implications for emerging technologies and electroceramic materials. By adjusting the concentration of these defects, we can fine-tune the properties of STO thin films. This tunability extends to various applications, including batteries, fuel cells, data storage, computer memories (such as Random-Access Memory or RAM), and more. This brief introduction provides an overview of the stoichiometry and non-stoichiometry of point defects in ionic crystal [2, 13, 14].

TABLE 2.1: Possible defects that can occur in crystalline solids

Geometrical Dimension	Type of Defect	Examples	Physical Properties
0	Point defects	doping, vacancies, interstitial	diffusion, conductivity
1	Line defect	edge, screw, dislocation	ductility, shear modulus
2	Planar defect	grain boundaries, twin boundary, stacking fault	texture, corrosion
3	Bulk defect	pores, cracks, voids, precipitates	porosity

2.2.1 Kröger-Vink-Notation

The Kröger-Vink-Notation is the international standard for describing defects. This notation system is used to describe electric charge and position of defects in crystal lattice. It employs the format M_S^C, where M denotes an atom or defect (e.g., V for vacancy). In the case of delocalized electronic defects, they can also represent electrons (e') or holes ($h^\bullet$). S indicates the lattice site where the defect is located; ’i’ represents an interstitial, or if it is occupied by an element, the symbol of that element must be written. C represents its effective charge. Positive charges are denoted by "•", negative charges by "′", and neutral charges by "x" (for more example see Table 2.2)[2, 15].

Table 2.2: Different types of defects, along with examples in Kröger-Vink notation

Defect type	**Kröger-Vink notation**	**Examples**
Vacancy	V_S	Oxygen vacancy ($V_O^{\bullet\bullet}$)
Interstitials	M_i	Cation interstitial ($Ba_i^{\bullet\bullet}$)
Foreign Atom	L_M	lower valance Y^{3+} taking site of Zr^{4+} (Y'_{Zr})

To define defects in chemical equations, we require three fundamental principles:

- Conservation of mass:

This rule ensures that the total mass of the reactants equals the total mass of the products in a chemical reaction. In the context of defect reactions, it emphasizes that the overall mass of the system should remain constant despite the occurrence of defects.

- Conservation of charge:

This rule focuses on the conservation of electric charge in a chemical reaction. It ensures that the total positive charge on the reactant side equals the total positive charge on the product side, and the same for negative charges. In the case of defect reactions, it implies that any changes in charge associated with defects must be accounted for to maintain overall charge neutrality.

- Conservation of site ratio (host structure):

This rule is specific to reactions involving defects in the crystal lattice or host structure of a material. It emphasizes the conservation of the ratio of different sites (positions) in the host structure. In other words, the arrangement of atoms or ions in the host lattice should remain consistent before and after the occurrence of defects [16].

2.2.2 Thermodynamic of point defects in ionic crystal structure

The formation of defects in a crystal becomes thermodynamically favorable as temperature increases. At absolute zero (0 K), an ideal crystal exists with minimal energy, but with higher temperatures, the Gibbs free energy decreases, making defect formation more feasible. This is because the creation of defects involves an enthalpy (ΔH) change, representing the energy cost associated with breaking and forming bonds. The interplay between enthalpy (ΔH) and temperature (T) in the Gibbs free energy Equation (2.1) leads to an increase in defect concentration as the temperature rises. However, while increasing temperature can elevate defect concentrations in a crystal, it's important to note that this increase is not infinite. Instead, defect concentrations can reach a critical point where further temperature elevation can lead to structural instability, potentially causing the crystal to collapse [14, 17, 18].

$$\Delta G = \Delta H - T\Delta S \tag{2.1}$$

The relationship between Gibbs free energy, entropy, and enthalpy is illustrated in Figure 2.2. The minimum of Gibbs free energy corresponds to a non-zero defect concentration, which represents the equilibrium concentration of defects in the crystal lattice [19].

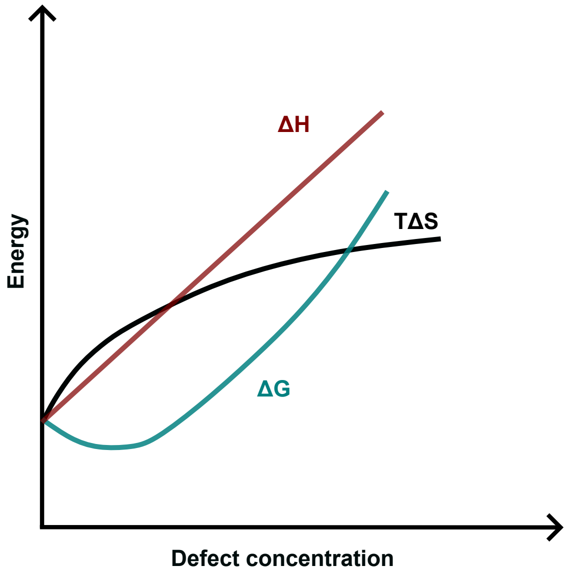

FIGURE 2.2: The interplay between Gibbs free energy, entropy, and enthalpy in thermodynamics for defect formation

Stoichiometric defects in ionic crystal structure

Two common stoichiometric types of defects in ionic crystals are due to Schottky and Frenkel disorders. In the case of Schottky disorder, an equal number of cations and anions are missing from their respective positions, leading to the formation of vacancy pairs. This maintains charge balance within the crystal lattice (see Equation (2.2)). This type of disorder is more likely in ionic crystals with closely packed ions. Figure 2.3 schematically illustrates the Schottky disorder in the crystal structure.

$$nil \longrightarrow \mathrm{V}_{M}'' + \mathrm{V}_{M}^{\bullet\bullet} \tag{2.2}$$

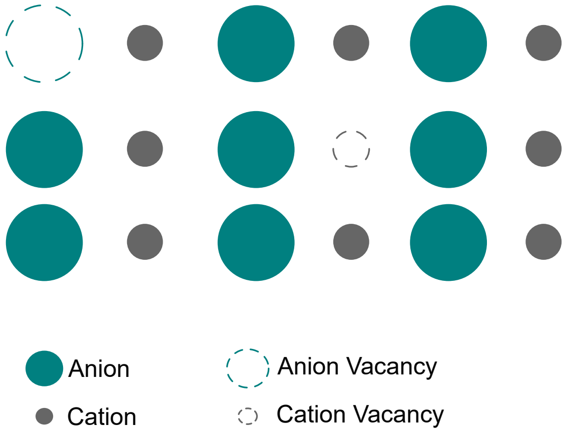

FIGURE 2.3: Schematic illustration of Schottky disorder in crystal structure

Frenkel type of point defects in crystalline solids results if an ion moves within the lattice, creating a vacancy plus an interstitial pair of atoms (see Equation (2.3)). It's called a Frenkel disorder if an anion moves and an anti-Frenkel disorder if a cation moves. These defects are more common in ionic crystals, where cations and anions have different sizes [20]. Figure 2.4 schematically illustrates the Frenkel and anti-Frenkel disorders in the crystal structure.

$$\mathrm{M}_M^X \longrightarrow \mathrm{M}_i^{\bullet\bullet} + \mathrm{V}_M'' \tag{2.3}$$

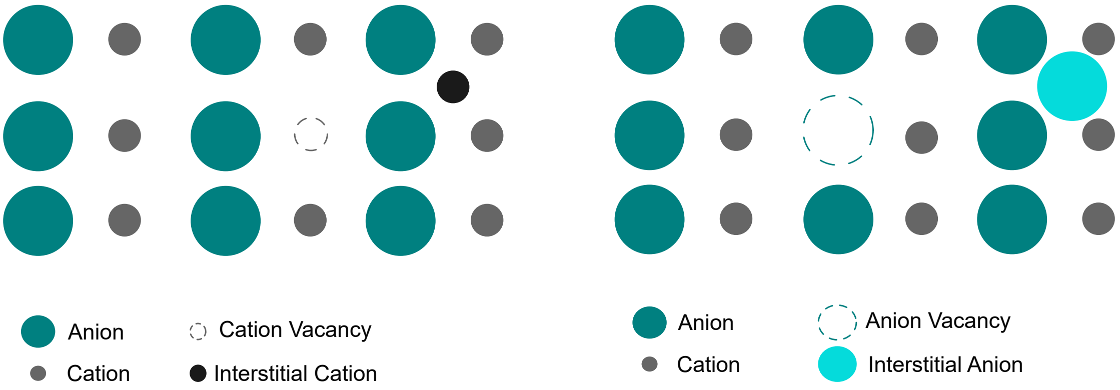

(a) Frenkel disorder

(b) anti-Frenkel disorder

FIGURE 2.4: Schematic illustration of Frenkel disorder in the crystal structure

Non-stoichiometric defects in ionic crystal structure

Non-stoichiometry refers to a deviation from the ideal stoichiometric ratio caused by changes in external conditions, such as alterations in the atmosphere or the presence of impurities. In non-stoichiometric crystals, an excess or deficit of cations or anions leads to charged defects, which are compensated by electronic or ionic defects to maintain charge balance. Extrinsic non-stoichiometry involves undesired impurities or the intentional addition of dopants to modify the material's characteristic behavior. Based on electronic contribution, dopants can be categorized as acceptors or donors.

Intrinsic nonstoichiometry is known as an ionic solid undergoes partial oxidation or reduction reactions due to changes in oxygen partial pressure (pO_2), leading to shifts in defect equilibrium and the generation of oxygen vacancies, electron holes, or other defects [15, 21].

The Brouwer diagram serves to approximate defect concentrations in dependence on the oxygen partial pressure. In simplified and generated terms, it can be divided into three regions (2.5 shows the schematic illustration of these regions):

- Region I: In this zone, metal oxides undergo reduction, resulting in oxygen vacancies becoming the primary ionic charge carriers, known as the n-type region. The electroneutrality equation can be expressed as:

  $$O_O^x \longrightarrow V_O^{\bullet\bullet} + e' + \frac{1}{2}O_2(g) \tag{2.4}$$

  $$[e'] = 2[V_O^{\bullet\bullet}] \tag{2.5}$$

  The slope of the Brouwer diagram for the oxygen vacancies concentration $[V_O^{\bullet\bullet}]$ is $-\frac{1}{6}$, whereas for the metal vacancies concentration $[V_M'']$, it is $\frac{1}{6}$. For the electron concentration $[e']$, the slope is $-\frac{1}{6}$, and $\frac{1}{6}$ for hole concentrations $[h^\bullet]$.

- Region II: This region has a stoichiometric point, where the dominant disorder type (Schottky, Frenkel, or intrinsic) determines the electroneutrality equation. For the Schottky defect, it can be represented as:

  $$[V_M''] = [V_O^{\bullet\bullet}] \tag{2.6}$$

  Near the stoichiometric point at lower partial pressure, oxygen vacancies are favored, while at higher partial pressure, cation vacancies are favored. The slope for the hole concentration $[h^\bullet]$ versus pO_2 is $\frac{1}{4}$, whereas for $[e']$, it is $-\frac{1}{4}$.

- Region III: In this area, metal oxidation occurs due to high oxygen partial pressure, and metal vacancies become the predominant ionic charge carriers. The electroneutrality equation is given by:

$$\frac{1}{2}O_2(g) \longrightarrow O_O^x + 2h^\bullet + V_M'' \tag{2.7}$$

$$2[V_M''] = [h^\bullet] \tag{2.8}$$

The slope of the Brouwer diagram for the oxygen vacancies concentration $[V_O^{\bullet\bullet}]$ is $-\frac{1}{6}$, while for the metal vacancy's concentration $[V_M'']$, it is $\frac{1}{6}$ and $-\frac{1}{6}$ for electron concentration $[e']$, $\frac{1}{6}$ is for hole concentrations $[h^\bullet]$ [14, 20, 22].

The Brouwer diagram can be calculated for various temperatures and different materials.

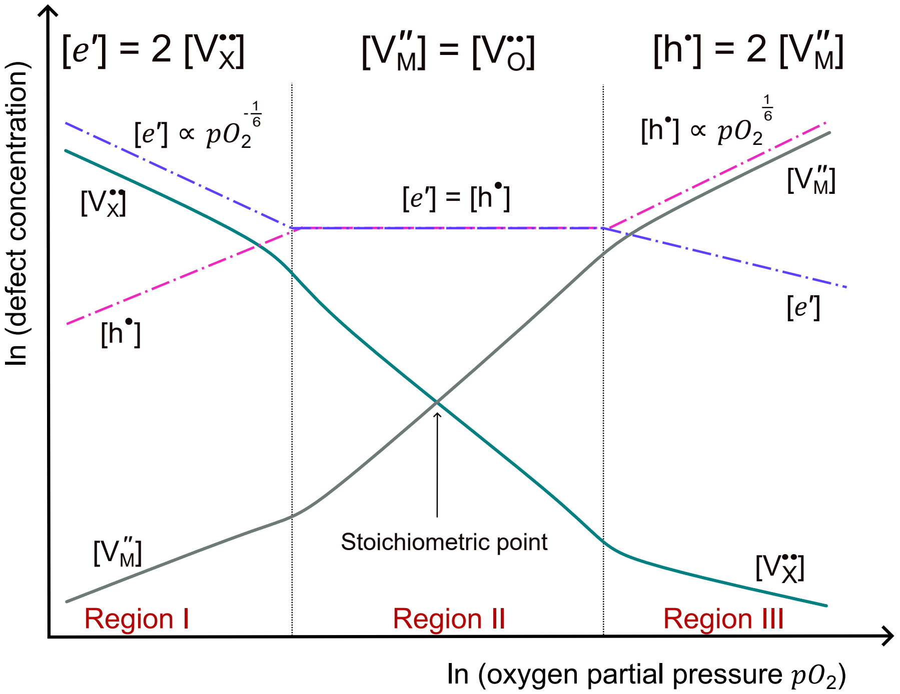

FIGURE 2.5: Schematic illustration of Brouwer diagram

2.3 Defects in STO

Defects in strontium titanate have been well investigated. STO is considered a model material. Due to its closely packed perovskite structure, Frenkel disorder are hardly presented, because of their higher formation energies compared to Schottky disorder. Three Schottky disorders with similar formation energy are present in STO. Equation (2.9), Equation (2.10), and Equation (2.11) provide reaction equations about how these defects can be formed.

$$Sr_{Sr}^{x} + Ti_{Ti}^{x} + 3O_{O}^{x} \rightleftharpoons V_{Sr}'' + V_{Ti}'''' + 3V_{O}^{\bullet\bullet} + \mathrm{SrTiO_3} \tag{2.9}$$

$$Sr_{Sr}^{x} + O_{O}^{x} \rightleftharpoons V_{Sr}'' + V_{O}^{\bullet\bullet} + \mathrm{SrO} \tag{2.10}$$

$$Ti_{Ti}^{x} + 2O_{O}^{x} \rightleftharpoons V_{Ti}'''' + V_{O}^{\bullet\bullet} + \mathrm{TiO_2} \tag{2.11}$$

Equation (2.9) is a full Schottky disorder present in STO. Equation (2.10) and Equation (2.11) are known as partial Schottky defects because they do not preserve the stoichiometry of the perovskite structure. The partial Schottky disorder includes SrO as a secondary phase. Sr vacancies described in Equation (2.10) can be activated during sample preparation. They become mobile when STO is prepared at temperatures around 1200°C, below this temperature, Sr vacancies are immobile and become frozen [23–26].

STO is also considered a mixed ionic-electronic conductive material. In various investigations of this study, we took advantage of this property, which allows for changes in oxygen nonstoichiometry (δ), resulting in changes in the intrinsic electronics of the material. In undoped STO material, mobile defects include oxygen vacancies and electronic defects. Equation (2.12) demonstrates the interaction of oxygen uptake by occupying oxygen vacancies. To ensure electron mobility, either two electrons e' needed to accompany the oxygen uptake (see Equation (2.12)) or two holes $h^{\bullet}$ to be generated (see Equation (2.13)) [27, 28].

$$\frac{1}{2}O_2 + V_{O}^{\bullet\bullet} + 2e' \rightleftharpoons O_{O}^{x} \tag{2.12}$$

$$\frac{1}{2}O_2 + V_O^{\bullet\bullet} \rightleftharpoons O_O^x + 2h^{\bullet} \tag{2.13}$$

Electronic defects arise through the coupling of electron-hole formation or their recombination (Equation (2.14)) [29].

$$\text{nil} \rightleftharpoons h^{\bullet} + e' \tag{2.14}$$

By substitutional doping of the A or B-site, the electronic conductivity of STO can be tailored. For instance, doping Nb^{5+} at the A-site (replacing Ti^{4+}) results in the generation of electrons and Sr vacancies, making it an n-type conductor, which conducts only electrons. Conversely, doping with Fe^{3+} at this site transforms STO into a p-type material by generating extra holes and oxygen vacancies, thereby enabling primarily the conduction of oxygen ions (cationic defects are minority [24, 30].

$$Nb_{Ti}^x \rightleftharpoons Nb_{Ti}^{\bullet} + e' \tag{2.15}$$

$$Fe_{Ti}^x \rightleftharpoons Fe_{Ti}' + h^{\bullet} \tag{2.16}$$

2.4 Sol-gel method

The sol-gel method stands as a well-investigated process in material science, providing a flexible way to tailor many materials with diverse applications. Initially, the sol-gel process was explored for oxide materials like glass and ceramics, it has applications now for the production of a wide range of materials such as organic, inorganic, and composite materials. This method finds usage in industrial production, such as advanced coatings like anti-corrosion [31, 32], or as an anti-reflective coat for solar cells [33]. Sol-gel processes also have application in producing nanomaterials like TiO_2 nanoparticles [34, 35], magnetic and electronic ceramics [36], and more. This method offers advantages compared to traditional approaches for producing glass or ceramic materials, such as high purity and low-temperature production, as well as reproducibility [37]. In this study, we employed the sol-gel method to fabricate of STO thin films, which offers advantages over physical deposition methods like PLD (Physical Laser Deposition) due to its lower cost.

A sol is a stable colloidal suspension of solid particles in a liquid, where the solid particles have diameters ranging from 1 to 100 nm. These solid particles can be metal alkoxides or polymers, while the liquid medium can be water (referred to as aqua sol-gel method) or organic solvents such as alcohol (known as non-aqua sol-gel method). The formation of the sol requires dispersion forces to exceed gravitational forces. A gel is defined by its three-dimensional interconnected network with pores within the liquid medium. It can consist of colloidal sol particles or macromolecules, referred to as colloidal and polymeric gels, respectively. The structure of the gel network, particularly in polymeric gels, can be categorized into four types:

1. Regular, layered arrangement (well-ordered lamellar structure)
2. Disordered covalent polymeric networks, with a lack of any ordered structure
3. Predominantly disordered polymer network formed through physical aggregation, where the network arises from physical interactions
4. Partially disordered structure [37, 38].

The aquas sol-gel process includes four main steps: 1) Hydrolysis 2) Condensation 3) Aging 4) Drying.

During the hydrolysis step of the aqua sol-gel process, the metal alkoxide and the solvent are mixed, resulting in the removal of the alkoxide functional group from the metal alkoxide and the generation of an alcohol functional group. The schematic chemical reaction can be written as follows:

$$M - OR + H_2O \longrightarrow MOH + ROH \tag{2.17}$$

where M is the metal and R the alkyl group (C_nH_{2n+1})

The hydrolysis step is followed by a condensation process, during which water or alcohol molecules are removed from the solution to form a gel by establishing metal oxide linking bonds (metal-oxo-metal). The quantity of water can alter the structure of the polymer branches and therefore the porosity, by affecting the number of metal-oxo-metal bonds, which can be also influenced by the addition of acid, base, or alkoxide precursors. The reaction can be generally written as:

$$M - OH + XO - M \longrightarrow M - O - M + XOH \tag{2.18}$$

The aging step is a continuation of the polycondensation step and reforms the gel network. Duration of the aging process can result in a decrease of the porosity by increasing the thickness of interparticle connections. The drying method employed can significantly alter the structure of the gel network and, consequently, the final network structure of the material. Various methods exist for removing the liquid from the porous medium, including thermal drying, freeze-drying, and supercritical drying. Thermal drying can cause the collapse of the gel structure, resulting in the formation of a xerogel. To prevent significant shrinkage, freeze-drying presents a superior alternative. Freeze-drying operates at lower temperatures, resulting in a structure known as a cryogel. Supercritical drying preserves the gel network structure while maintaining high porosity and surface area [39, 40].

2.5 Electrochemical Impedance Spectroscopy (EIS)

EIS stands as a powerful nondestructive technique for measuring electrochemical phenomena within diverse systems containing charge carriers such as electrons or ions. EIS finds applications across various research, including biosensing [41], corrosion [42], battery technology, solid oxide fuel cells (SOFCs), and more. Despite its utility, EIS is based on a complex mathematical background. Herein is a brief introduction to its measurement principles.
Ohm's law defines the behavior of a perfect resistor through Equation (2.19), where V represents the voltage (volts), I (amps) stands for the current, and R (Ω) denotes the resistance of the current flow.

$$R = \frac{V}{I} \tag{2.19}$$

By employing EIS measurements, a sinusoidal voltage or current is applied to the system at a selected frequency. The Ohm's law can be expressed accordingly, as shown in Equation (2.20), wherein instead of 'R', 'Z' is utilized to represent impedance (Ω), with 'E(ω)'(volt) denoting the alternating current (AC) potential and 'I(ω)'(amps) representing the AC. When a sinusoidal potential serves as the input to the system (and the output is impedance), it is referred to as Potentiostatic EIS (PEISP). Conversely, when the input is current, it is termed Galvanostatic EIS (GEIS).

$$Z = \frac{E(\omega)}{I(\omega)} \tag{2.20}$$

A sinusoidal potential (E) as the input exhibits wave-like behavior. Figure 2.6 a) illustrates the wave behavior of the input potential at $t = 0$, while Figure 2.6 b) shows a possible output wave signal corresponding to the input signal.

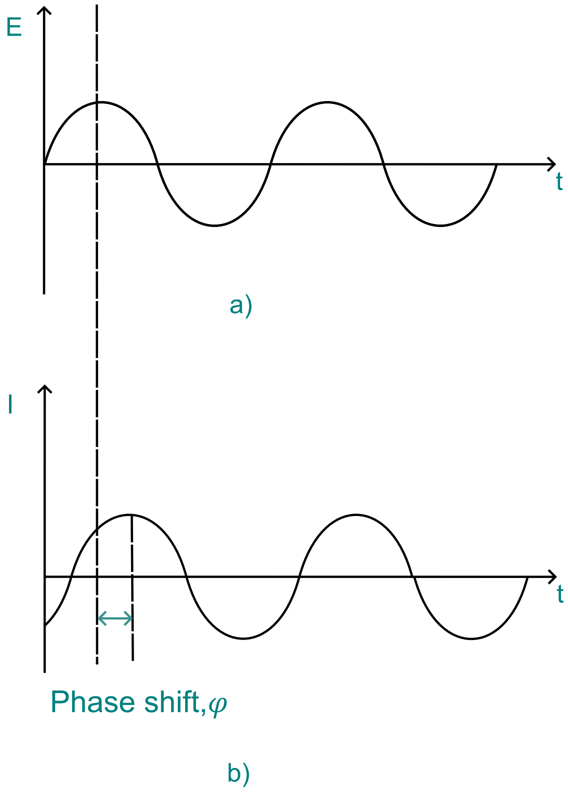

FIGURE 2.6: The sinusoidal waveform response within a linear system reveals a phase-shift angle used for describing electrochemical reactions. a) Input voltage with a certain frequency, b) Output response from sample

In this representation, the two waves exhibit a constant time shift. This is called a phase-angle shift (φ). Thus, the equation for the input potential as a function of time can be expressed as:

$$E_t = E_0 \sin(\omega t) \tag{2.21}$$

The potential at time "t" (denoted as E_t) is determined by the amplitude of the signal (E_0) and the angular frequency (ω) is measured in radian per second.

To maintain the linear characteristics in electrochemical systems, typically a low amplitude of alternating current (AC) voltage, ranging from approximately 5 to 10 mV, is employed. Considering the phase shift, the equation for the output current as a function of time can be written as:

$$I_t = I_0 \sin(\omega t + \varphi) \tag{2.22}$$

where I_t in a singular response of instantaneous current at its maximum amplitude, I_0 is the distinct amplitude of the output signal. φ represents the phase angle shift.
Referring to Ohm's law (Equation (2.20)), we can reformulate it using Equation (2.21) and Equation (2.22).

$$Z = \frac{E_0 \sin(\omega t)}{I_0 \sin(\omega t + \varphi)} = Z_0 \frac{\sin(\omega t)}{\sin(\omega t + \varphi)} \tag{2.23}$$

where the characteristic impedance (Z_0) is the ratio between the applied voltage (E_0) and the current (I_0). Given the identical frequency (ω) of the input and output signals in a linear time-invariant (LTI) system, both signals can be interconnected through a transfer function Z (ω) as a function of frequency with the imaginary unit $j = \sqrt{-1}$.

$$Z(\omega) = |Z_0| \exp^{j\varphi} = |Z_0|(\cos \varphi + j \sin \varphi) \tag{2.24}$$

Consequently, the impedance at this frequency Z (ω) expressed as:

$$Z(\omega) = Z' + jZ'' \tag{2.25}$$

A Nyquist plot is plotting the real component (Z′) against the imaginary component (Z′′). In a Cartesian coordinate system, the real component (Z′) can be plotted on the x-axis, representing the resistance, while the imaginary component (Z′′) can be plotted on the y-axis, depicting the reactance. This presentation of the impedance is commonly referred to as a Nyquist plot. The absolute value of impedance, referred to as modulus, is illustrated as a vector with a phase shift $\varphi = \omega t$. Figure 2.7 illustrates the impedance at one certain frequency as a vector concept.

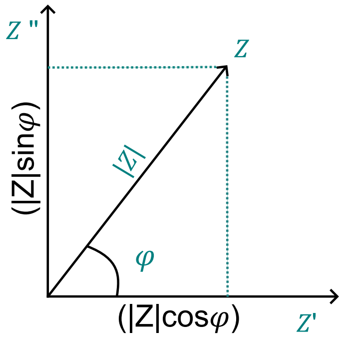

FIGURE 2.7: Representation of the impedance as a complex vector, the x-axis is the imaginary part and the y-axis is the imaginary part

$$Z' = |Z| cos\varphi \tag{2.26}$$

$$Z'' = |Z| sin\varphi \tag{2.27}$$

$$|Z| = \sqrt{(Z')^2 + (Z'')^2} \tag{2.28}$$

$$\varphi = tan^{-1}\left(\frac{Z''}{Z'}\right) \tag{2.29}$$

Additionally, Bode plots offer two distinct graphical representations to extract further insights from the measured electrochemical system. These plots present the modulus of impedance Z against frequency and the phase-angle (φ) [42–44].

In practice, commonly used frequency ranges are between 1 MHz to 10 mHz. This allows for the differentiation between various time dependence electrochemical phenomena, such as diffusion and ion conduction in electrolytes. Slower electrochemical processes are effectively probed at lower frequencies, whereas faster processes are better examined at higher frequencies. By leveraging this frequency-dependent approach, researchers can gain a comprehensive understanding of the underlying mechanisms governing electrochemical behavior. Measured data can be described and fitted by the use of equivalent circuit elements.
Measured data are typically conducted from high frequency to low frequency. Figure 2.8 illustrates the Nyquist plot for the most used circuit elements.
In Figure 2.8a despite an ideal resistor, which manifests as a single point lying on the real axis. This is because the real part being represented by R and its imaginary part being 0. Therefore, the position along the x-axis corresponds directly to the resistance value of the resistor.
Figure 2.8b presents an ideal capacitor, resulting in a straight line along the imaginary axis. Here, the real part of the impedance is zero, while the imaginary part is proportional to $1/(\omega C)$.

The depiction of a parallel RC-element is demonstrated in Figure 2.8c, where the Nyquist plot appears as a perfect semicircle. This parallel RC-element comprises a resistor and a capacitor in parallel. At high frequencies ($\omega \rightarrow \infty$), the current predominantly flows through the capacitor, while at low frequencies ($\omega \rightarrow 0$), the current primarily passes through the resistor due to the absence of capacitive effects. This transition from predominantly capacitive to predominantly resistive behavior results in the characteristic semicircular shape of the Nyquist plot.

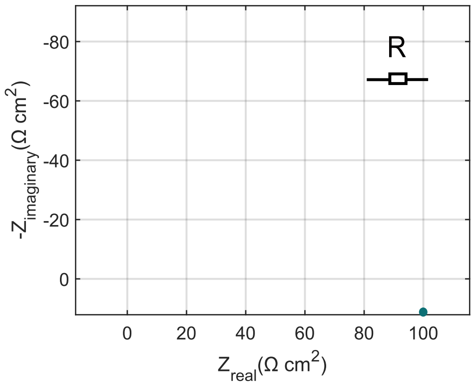

(a) Ideal resistor

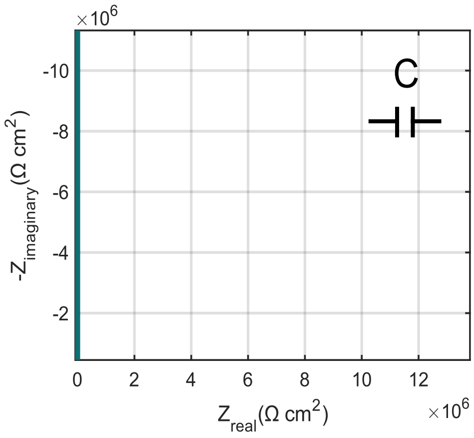

(b) Ideal capasitor

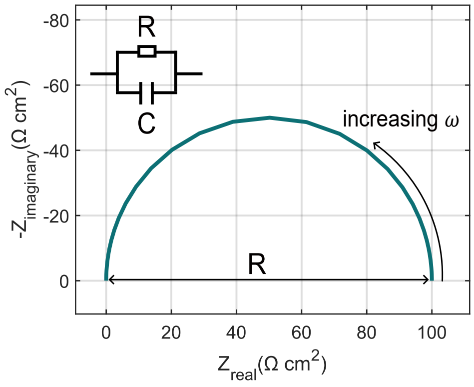

(c) Parallel RC-element

Figure 2.8: Nyquist plots of commonly used circuit elements with their corresponding equivalent circuit models

3 Experimental

3.1 List of chemicals

Table 3.1: List of chemicals used in this work

Chemical Formula	Name	Purity(%)	Supplier
$EtOH$	Ethanol	99.98	Sigma Aldrich
$Ti(OCH_2CH_2CH_2CH_3)_4$	Titanium(IV)butoxide	97	Sigma Aldrich
$Sr(CH_3CO_2)_2 \cdot 0.5H_2O$	Strontium acetate hemihydrate	98	Alfa Aesar
$CH_3COCH_2COCH_3$	Acetylaceton	98	Sigma Aldrich
CH_3COOH	Acetic acid	100	Sigma Aldrich
CH_3OCH_2CH2OH	2-Methoxyethanol	99.8	Sigma Aldrich
Pt	Platinum paste	-	Tanaka
$La_{0.6}Sr_{0.4}FeO_{3-\delta}$	LSF paste	-	-
$Gd_{0.1}Ce_{0.9}O_{2-\delta}$	GDC	-	Treibacher
$Y_{0.17}Zr_{0.83}O_{1.915}$	9.5 mol% YSZ single crystal (100)	-	Mateck
$Nb\text{-}doped\ SrTiO_3$	0.5 wt% Nb:STO single crystal (100)	-	CrysTec
O_2	Oxygen gas	99.999	Messer

3.2 Sol-gel synthesis

3.2.1 Strontium titanate precursor preparation via sol-gel process

The sol-gel process for the preparation of the STO thin film was employed according to Liu et al. [5], however, the heating treatment to achieve crystallization of the STO thin film was altered and will be described throughout this section. Titanium tetrabutoxide and strontium acetate hemihydrate were chosen as the starting materials for the precursor. To achieve a 1:1 ratio of strontium (Sr) to titanium (Ti), 0.2 M solution of titanium tetrabutoxide in 2-methoxyethanol and another 0.2 M containing strontium acetate in acetic acid were prepared. Strontium acetate was first dissolved in hot acetic acid (60 °C) under constant stirring, and the resulting solution was stirred for half an hour until it became clear and colorless. Titanium tetrabutoxide was dissolved in 2-methoxyethanol in the room temperature and stabilized using a few drops of acetyl acetate. After the strontium solution was cooled down to room temperature, the titanium solution was added dropwise. The mixture was then stirred for 6 hours and followed by aging for 24 hours. A schematic illustration of the preparation of the precursor is shown in Figure 3.1.

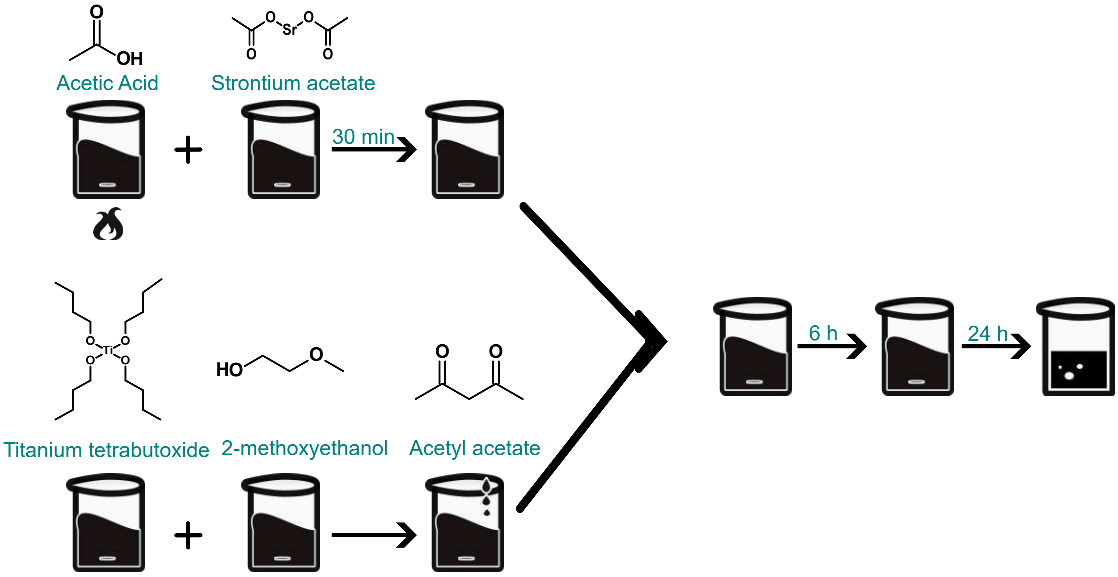

Figure 3.1: Schematic illustration of the precursor preparation for the STO thin films

3.2.2 Production of strontium titanate thin film layers

To obtain STO thin films, 50-100 µL of the solution was dispensed onto the YSZ single crystal substrate by using spin-coating for 15 seconds at 5400 rpm. Subsequently, the sample was dried at 150 °C on a hot plate for 3 min, followed by pyrolysis at 450 °C for 5 min on the hot plate. To achieve a desired film thickness of approximately 200 nm, the spin coating process and heating sequence was repeated eight times. The STO thin film was subsequently annealed in an air atmosphere furnace. The furnace was gradually heated at rate of 10 °C per minute and at the desired temperatures was maintained for 3 hours (for analytical analysis the temperature was varied from 550 °C to 850 °C and for electrochemical analysis a temperature of 850 °C was chosen; more details will follow). Subsequently, the STO thin films were cooled down at a rate of 10 °C per minute. A schematic illustration of the heating process is shown in Figure 3.2.

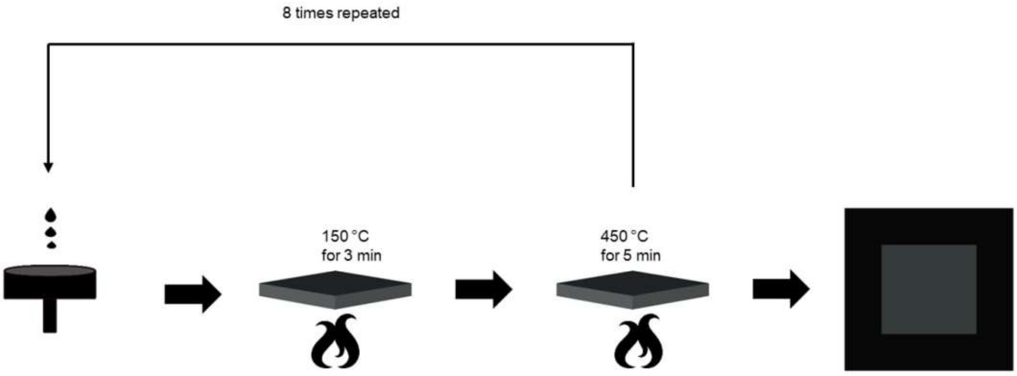

FIGURE 3.2: Schematic illustration of the heat treatment and the annealing of crystalline STO thin film to achieve a film thickness of 200 nm

3.3 Sample preparation

3.3.1 Sample preparation for analytical analysis

The goal of this study is to analyze STO thin films, which are prepared by the sol-gel process. The characterization will be split into two main categories: 1) the analytical and 2) the electrochemical characterization. For the analytical characterization, four main samples were explored:

1. Exploration of the effect of the annealing temperature on STO thin films: STO precursors synthesized via the sol-gel process were deposited onto YSZ substrates and subjected to a heat treatment, followed by annealing at temperatures ranging from 550 °C to 850 °C for 3h.
2. Influence of the precursor aging on STO thin films: Following synthesis via the sol-gel process, STO precursors were aged for durations of 48 hours, one month, and three months. Subsequently, they were deposited onto YSZ substrates and subjected to a heat treatment, followed by annealing at 850 °C for 3h.
3. Exploring different Sr:Ti ratios: Three batches were prepared. The first batch contained 1M strontium and 2M titanium solutions, resulting in a ratio of 0.5 parts strontium to 1 part titanium. Another batch was prepared with a 1:1 ratio of strontium to titanium. The third batch included 4M strontium and 2M titanium solutions, yielding a ratio of 2 parts strontium to 1 part titanium. These batches were then used to create STO thin films using the sol-gel process, followed by a heat treatment and annealing at 850 °C for 3h.
4. Reproducibility of the method: STO precursors synthesized via the sol-gel process were deposited onto YSZ and annealed at 850 °C for 3h. This procedure was repeated three times to evaluate reproducibility.

The methods utilized for the analytical characterization were Scanning Electron Microscope (SEM), GIXRD, LA-ICP-MS, and Atomic Force Microscopy (AFM).

3.3.2 Sample preparation for electrochemical analysis

STO thin film on YSZ for measurement under bias voltage

Impedance measurement under bias voltage were carried out on a sample with an oxygen ion-buffer as a counter electrode, an electrolyte (YSZ), and a working electrode (STO) (see Figure 3.3). The fabrication of an oxygen-ion buffer was the first step for the preparation of the impedance measurement under bias voltage. The oxygen ion-buffer counter electrode, was made up of 80 wt% Gd:CeO_2 (GDC) (consist of GDC powder and a Terpineol based ink vehicle) and 20 wt% Fe_2O_3, dispersed in an ink vehicle at a 1:1 weight ratio and homogenized in a rotary ball mill (Fritsch Pulverisette)). GDC/Fe_2O_3 was spin-coated onto the back side of a $5 \times 5 \times 0.5\,mm^3$ YSZ. The spin-coating process was carried out at 2400 rpm for one minute and then dried in a dry cabinet at 100 °C. Subsequently, a thin layer of Pt paste was brushed on top of GDC/Fe_2O_3 and the sample was sintered at 1050 °C for 3 hours [45]. After preparation of the back side of the YSZ, a STO thin film as (working electrode) was grown on the top side of YSZ by the sol-gel process as previously explained in Section 3.2. This was followed by sputtering a current collector consisting of 5 nm Ti (adherence layer) and 250 nm Pt onto the STO thin film. The metalic thin film of Ti/Pt metal was deposited using the metal sputtering method. The sample chamber was initially evacuated to 10^{-5} mbar and subsequently set to the specified Argon pressure. Fisrt the Ti layer was deposited onto the sample through sputtering, followed by sputtering of the Pt layer over the Ti layer. Table 3.2 shown exact parameter for sputter process.

Table 3.2: Metal Sputtering Parameters

	Titanium	**Platinum**
Sputter time (s)	55	403
Argon pressure (mbar)	7.10^{-3}	2.10^{-2}
Sputter current (mA)	100	100

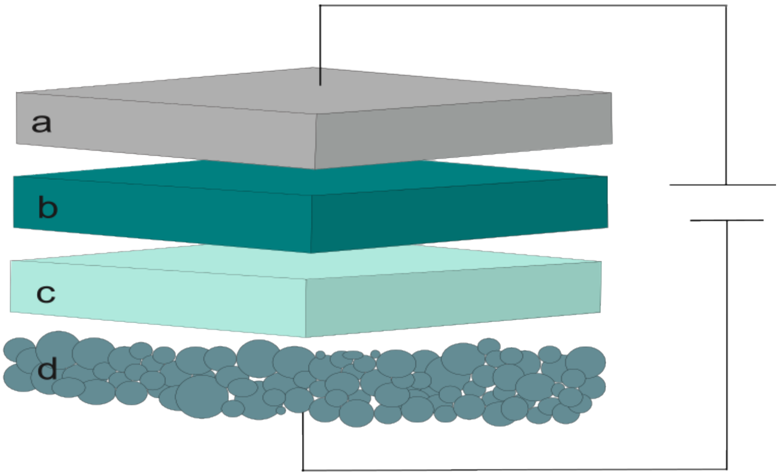

FIGURE 3.3: Schematic illustration of a sample prepared for the impedance measurement under bias a) Current collector (Ti/Pt) b) Working electrode (STO) c) Electrolyte (YSZ) d) Counter electrode (GDC/Fe_2O_3, spin coated) with a Pt layer on top (brushed)

STO thin film on Nb:STO for conductivity measurements

To measure the conductivity of the STO thin film, a sample with Nb:STO as a substrate was required. The STO sol-gel precursor was spin-coated onto the polished side of a $5 \times 5 \times 0.5\,\mathrm{mm}^3$ Nb:STO single crystal (spin-coating process was previously explained in Section 3.2). Afterward, Pt paste was brushed onto the unpolished side of the Nb:STO and dried in a drying cabinet for 15 min at 100 °C. The Pt paste was sintered simultaneously during the STO annealing process. Pt microelectrodes were applied to the STO working electrode using photolithography and metal sputtering. Photolithography was done in a dust-free room. The sample was initially wiped with ethanol and blow-dried with nitrogen gas. The procedure involved applying 100 µL of ma-N 1420 Photoresist Laquer (MicroResist Technology, Germany) onto the samples using an SCC-200 spincoater (KLM, Germany). Subsequently, the coated sample was dried on a hot plate for 4 min at 100 °C. Following this, the sample was exposed to UV light (350 W, USHIO 350DP Hg, Ushio, Japan)(detailed information in Table 3.3) through a patterned shadow mask, that features circular microelectrodes with diameters ranging between 50–1000 µm. Areas of the photoresist, that were not exposed to UV light, were then removed using a ma-D 533/s developer solution (Microresist Technologies, Germany) and the residual developer solution was removed by submerging the sample in deionized water. Consequently, a thin layer of Ti/Pt (with 5 nm Ti and 100 nm Pt thickness) was sputtered according to the procedure detailed in

Table 3.4 on the STO thin film, with the dried photoresist on top. The sample was then carefully submersed in ethanol to remove the remaining of the photoresist. A schematic illustration of the sample geometry is shown in Figure 3.4.

TABLE 3.3: Photolithography parameters

Photoresist (µL)	100
Spin coater program (rpm, s)	(100, 40) followed by (60, 15)
Heating temperature (°C)	100
Heating duration (min)	4
UV light exposure (s)	60
Developing time (s)	60 to 120

TABLE 3.4: Metal Sputtering Parameters

	Titanium	**Platinum**
Sputter time (s)	55	161
Argon pressure (mbar)	7.10^{-3}	2.10^{-2}
Sputter current (mA)	100	100

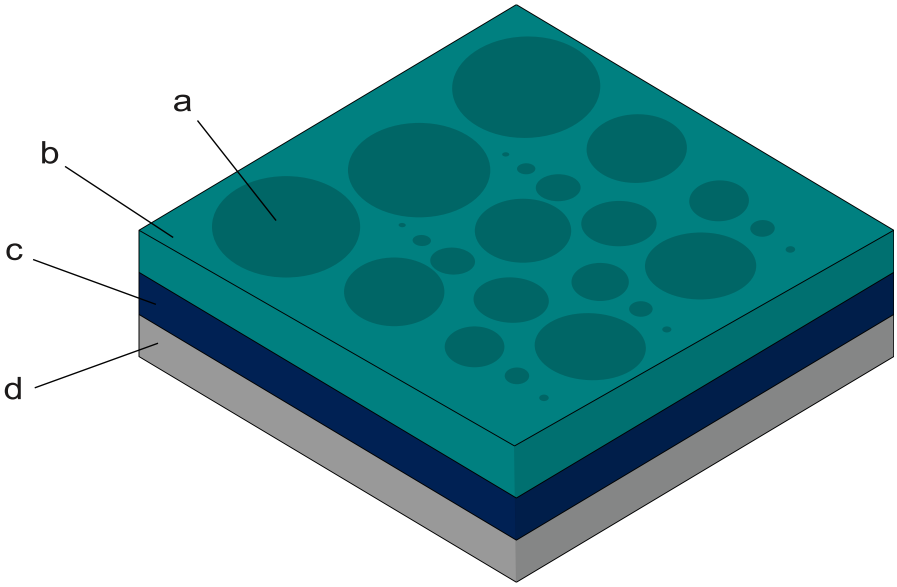

Figure 3.4: Schematic illustration of the sample prepared for the conductivity measurements a) Microelectrode (Ti/Pt) b) Working electrode (STO) c) Nb:STO single crystal d) Porous Counter electrode (Pt paste)

Half cell battery

To measure the STO thin film layer as a half-cell battery, we needed a desired configuration of the sample. We designed the setup with the reference electrode placed opposite the working electrode to measure the overpotential of only the counter electrode. The STO thin film (working electrode) was deposited on YSZ (elektrolyt). On top of the STO thin film layers of current collector (Ti/Pt) were sputtered and additionally covered with glass layer to prevent the oxygen uptake from the surrounding atmosphere Figure 3.5. A counter electrode ($La_{0.6}Sr_{0.4}FeO_{3-\delta}$ (LSF)) and reference electrode (also LSF) were brushed on the bottom side of the substrate.

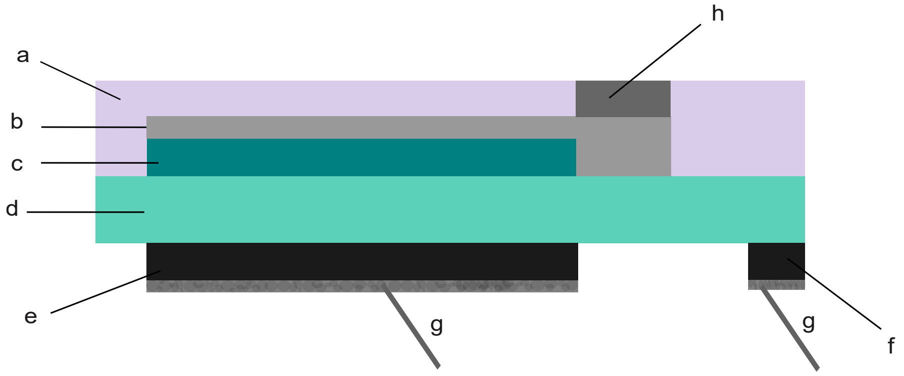

Figure 3.5: Schematic illustration of a battery cell a) Glass paste b) Current collector Ti/Pt c) Working electrode (STO) d) Electrolyte (YSZ) e) Counter electrode (LSF) with Pt paste f) Reference electrode (LSF+Pt) on top g) Ti wire h) Pt paste for connecting the working electrode

STO was spin-coated with the same procedure explained earlier in Section 3.2 on to the YSZ single crystal using a mask made from Kapton tape with cutout size of 6×8 mm^2. The Kapton tape was precisely cut using a precision cutting plotter (Roland Versastudio GS2-24). Kapton tape is a polyamide with silicon adhesive. Notably, the silicon carries potential toxicity for surface reactions. This mask was placed on a YSZ single crystal substrate measuring $10 \times 10 \times 0.5$ mm^3.

An alternative approach to the heat treatment of the STO precursor was employed following the spin coating, due to the loss of Kapton tape's adhesive properties beyond 350 °C. As mentioned former, after spin-coating, the sample was initially heated for 3 minutes at 150 °C (drying step), followed by a subsequent heating for 5 minutes at 450 °C (pyrolysis step). This process was repeated eight times to achieve approximately 200 nm of STO thin film. Moreover, heat of the Kapton mask above 450 °C causes the Kapton to lose its adhesive properties, which means that the heat treatment of the STO thin film can not exceed the 450 °C for pyrolysis step.

To address this issue, only the drying process at 150 °C was employed after spin-coating and repeated eight times. Subsequently, the Kapton layer was removed, and the sample subjected to pyrolysis at 450 °C for 5 minutes.

On the back side of the YSZ single crystal, a layer of LSF paste was brushed, using a nominally identical Kapton mask to precisely apply LSF and ensured the alignment with the STO (working electrode on top of the YSZ). Additionally, a small amount of LSF was applied at the corner as a reference electrode. After allowing the LSF to dry for 30 minutes in a drying cabinet, Pt paste was applied on LSF and dried for 10 minutes. STO and the brushed LSF/Pt layer were sintered simultaneously at 850 °C.

A Ti/Pt layer (5 nm Ti and 100 nm Pt thickness) was applied onto the STO layer, extending approximately 1 mm beyond the STO layer on the YSZ single crystal substrate, the subsequent procedure is outlined in Table 3.4. (Figure 3.6 shows the Ti/Pt on top of the STO layer on YSZ)

Figure 3.6: Microscopic image of a half-cell battery featuring a Ti/Pt thin layer coating atop an STO thin film (highlighted in red with area of 35.85 mm^2), placed on the YSZ single crystal

Pt wires were securely attached with Pt paste onto both the counter electrode and reference electrode for measurement purposes. The Ti/Pt film coated STO thin film was sealed using a glass layer. For this purpose, glass paste was brushed on STO thin coated with Ti/Pt layer onto top of the YSZ. A small point of the Ti/Pt sputtered layer was left uncovered by the glass paste, allowing for connection, and was instead brushed with Pt paste. This step was done to ensure the electrical contact with STO as working electrode. Subsequently, the setup was subjected to sintering at 700 °C for half an hour with a heating rate of 9 °C/min and then gradual cooling at 1.9 °C/min.

3.4 Analytical and electrochemical measurement methods

3.4.1 Analytical methods

Scanning Electron Microscope (SEM)

SEM images were acquired using the SEM instrument at USTEM - Elektronenmikroskopie, TU Wien, employing a Quanta 250 FEG (FEI, USA). Due to the low conductivity of all samples, a thin layer of Pd-Au was sputtered onto all samples to ensure uniform conductivity and achieve optimal image quality.

Grazing Incidence X-ray Diffraction (GIXRD)

GIXRD functions by using a small incident angle X-ray beam to minimize penetration into the samples, making it a sufficient method for the thin film analysis. GIXRD measurements were conducted at the XRC — X-Ray Center at TU Wien, utilizing an Empyrean X-ray diffractometer (PANalytical, United Kingdom) with a PIXcel3D detector (Malvern Panalytical Ltd.) and a parallel beam mirror on the incident beam side with a scintillation detector on the diffracted beam side. Scans were performed on all samples for angles between $\theta - 2\theta(20 - 90°)$.

Laser Ablation Inductively Coupled Plasma Mass Spectrometry(LA-ICP-MS)

The LA-ICP-MS setup consists of a Thermo Scientific™ iCAP™ TQ ICP-MS system (Thermo Fisher Scientific, Bremen, Germany) and a NWR213 laser ablation system (ESI, Fremont, USA), connected by PTFE tubing with 2 mm inner diameter. LA-ICP-MS conditions are given in Table 3.5. The measurements were conducted using an STO (100) single crystal as a reference for one-point calibration. Each sample was scanned at five distinct locations with the laser, resulting in ablated lines totaling 1 mm in length. The laser spot dimensions were configured at 10 µm x 10 µm with no overlap, while maintaining a laser fluence of 2.59 J/cm^2 and a repetition rate of 10 Hz.

Table 3.5: LA-ICP-MS measurement condition

Plasma Power (W)	1550
Dwell time(s)	0.1
Nebulizer gas flow (Ar) (L/min)	1
Cool gas flow (Ar) (L/min)	14
Auxiliary gas flow (L/min)	0.8
Measurement mode	TQ-O_2
Collision/reaction gas flow (O_2)(mL/min)	0.33
Measured isotopes as oxides	47Ti, 48Ti, 86Sr, 87Sr

3.4.2 Electrochemical methods

STO thin film on YSZ for measurements under bias voltage

EIS measurement under bias voltage were conducted using the BioLogic SP200 potentiostat, which features a built-in impedance analyzer. The sample was positioned within a tube furnace on a Pt sheet, and connections between the counter electrode and the working electrodes were established using Pt-Ir needles. One needle was placed on top of the working electrode and the second was placed on the Pt sheet in order to connect the counter electrode. For temperature monitoring, a type-S thermocouple was placed approximately 1 cm below the sample holder (Figure 3.7 shows the schematic distance between sample holder and thermocouple). The connected sample was sealed within a silica outer tube from atmosphere and subsequently inserted into a tube furnace. Prior to the measurement under bias, the entire system was heated and evacuated overnight, to prevent any reaction between lab air contaminants or humidity with the sample. The furnace set temperature was 200 °C in order to have almost 100 °C inside the silica tube and sample.The outer chamber was heated using a heating wire to maintain a temperature of 100 °C overnight (Figure 3.7 shows a schematic illustration of the measurement setup and Figure 3.8 shows the photo of the measurement setup and a close up of the sample). Vacuum was established by using the Turbo-V70 pump with ISO 63 high vacuum flange (VARIAN Leini Torino ITALY), coupled with a vacuum pump (TRICAC type D, manufactured in GERMANY). Overnight, a vacuum level of 5×10^{-6} mbar was achieved.

The oxygen ion-buffer counter electrode has been used in order to precisely control the activity of oxygen in the working electrode. Prior to the EIS measurement, counter electrode conditioning was performed to reduce Fe_2O_3. The counter electrode conditioning was done by applying constant current of 56 μA to the cell for a duration of 30 minutes at 500 (±5) °C and

5×10^{-6} mbar pressure. By releasing O_2, Fe_2O_3 partially reduced to Fe/$Fe_{0.98}O$. Ultimately, the oxygen activity can be regulated by Fe/FeO phase equilibrium with

$$a(\mathrm{O}_2)_{CE} = \exp \frac{2\Delta_f G^0}{RT} \tag{3.1}$$

where $a(\mathrm{O}_2)_{CE}$ is the oxygen activity at the counter electrode (GDC/Fe/FeO), R is the universal gas constant (J/mol.K), T is temperature (K), and $\Delta_f G^0$ is the molar standard formation enthalpy of FeO $\Delta_f G^0 (J.mol^{-1})$ is [46]:

$$\Delta_f G^0 = -303.097 + 683.5T - 91.4TlnT + 0.05T^2 \tag{3.2}$$

where units of experimentally determined coefficients are $J.mol^{-1}$, $J.mol^{-1}.K^{-1}$, $J.mol^{-1}.K^{-1}$ and $J.mol^{-1}.K^{-2}$ respectively.

The oxygen activity of the working electrode (STO) can be determined from the cell voltage from Nernst's equation:

$$a(\mathrm{O}_2)_{WE} = \exp \frac{2\Delta_f G^0 + 4FU_{cell}}{RT} \tag{3.3}$$

where $a(\mathrm{O}_2)_{WE}$ is the oxygen activity at the working electrode (STO), U_{cell} is the applied voltage, and F is the Faraday constant. In previous publications, GDC/FeO was employed in a comparable cell design for the purpose of an oxygen release in XPS measurement [45, 47] and also as an oxygen sub-stochiometric GDC counter electrode [48]. However, this approach aims to provide a precise control over the release of oxygen for EIS measurement under bias voltage.

Impedance measurements were performed at a sample temperature of 500 (±5) °C and 5×10^{-6} mbar chamber pressure. Bias voltages ranging from -1 V to 1 V were applied at intervals of 10 mV. EIS measurements were subsequently conducted within the frequency range of 10 kHz to 20 mHz, utilizing an amplitude of 10 mV.

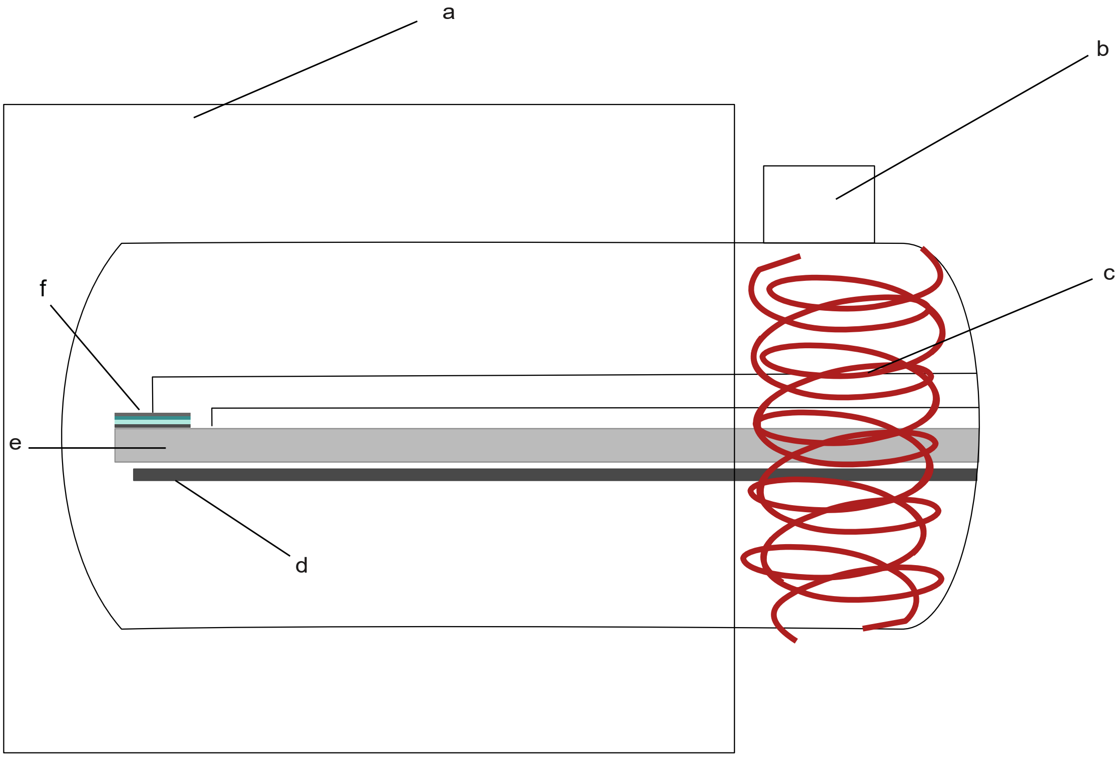

FIGURE 3.7: A schematic illustration of the measurement setup used for impedance measurements under bias voltage a) Furnace b) Turbo pump c) Heating wire around the outside of the chamber d) Thermocouple e) Sample holder, f) Sample

(a) The entire setup contains the furnace and outer tube covered with heating wire, that are shielded by an aluminum layer to prevent heat lost

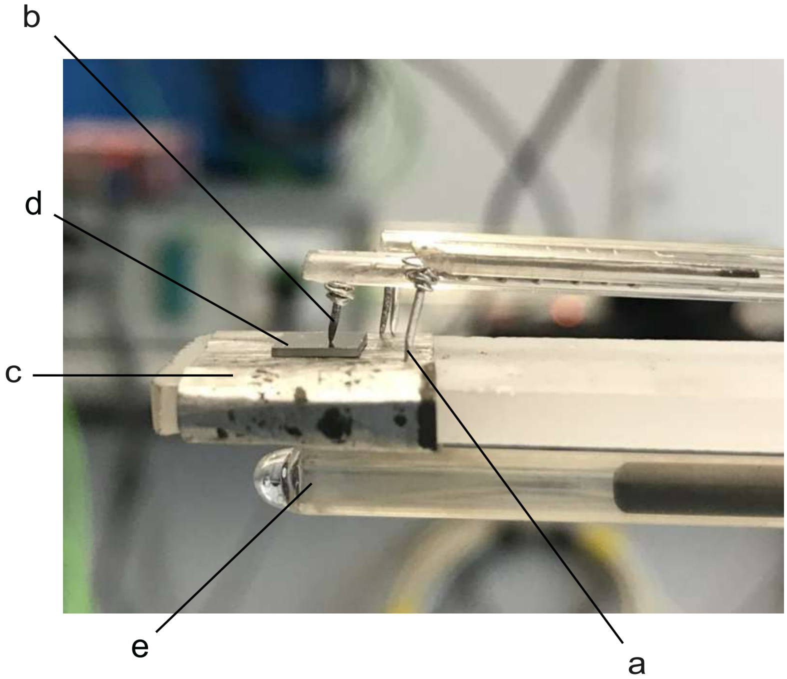

(b) A closer look at the sample placed on the sample holder a) Needle connected to counter electrode b) Needle connected to working electrode c) Pt-sheet on sample holder d) sample e) Thermocouple

FIGURE 3.8: a) Photo of the measurement setup used for impedance measurement under bias voltage and b) closer look of the sample

STO thin film on Nb:STO for conductivity measurements

Measurements for the analysis of the conductivity of STO thin film on Nb:STO were conducted using STO thin films grown on Nb:STO single crystal, as described in Subsection 3.3.2.

The measurement setup, similar to that utilized in measurements of the STO thin film under bias voltage, was also employed for this measurement. Microelectrodes, ranging in diameter from 300 to 700 µm, were positioned atop the working electrode (STO) and connected using Pt-Ir needles. One needle was positioned on top of the microelectrode, while the second one was placed on a Pt sheet on the sample holder to facilitate the connection between the working and counter electrodes (see Figure 3.9).

The samples were positioned within a uniformly heated furnace, maintaining a temperature range of 500 °C to 600 °C. Prior to the EIS measurement, 1 bar of oxygen gas was bubbled through the setup to allow equilibration of the sample with the atmosphere. Additionally, a constant flow of the oxygen gas during the measurement was used to prevent any reactions between lab air contaminants and the sample.

To assess the conductivity of the thin films, we employed electrochemical impedance spectroscopy with an Alpha-A High-Resolution Analyzer (Novocontrol, Germany), covering a frequency range from 1 MHz to 5 mHz with a resolution of 10 points per decade and an AC rms amplitude of 10 mV.

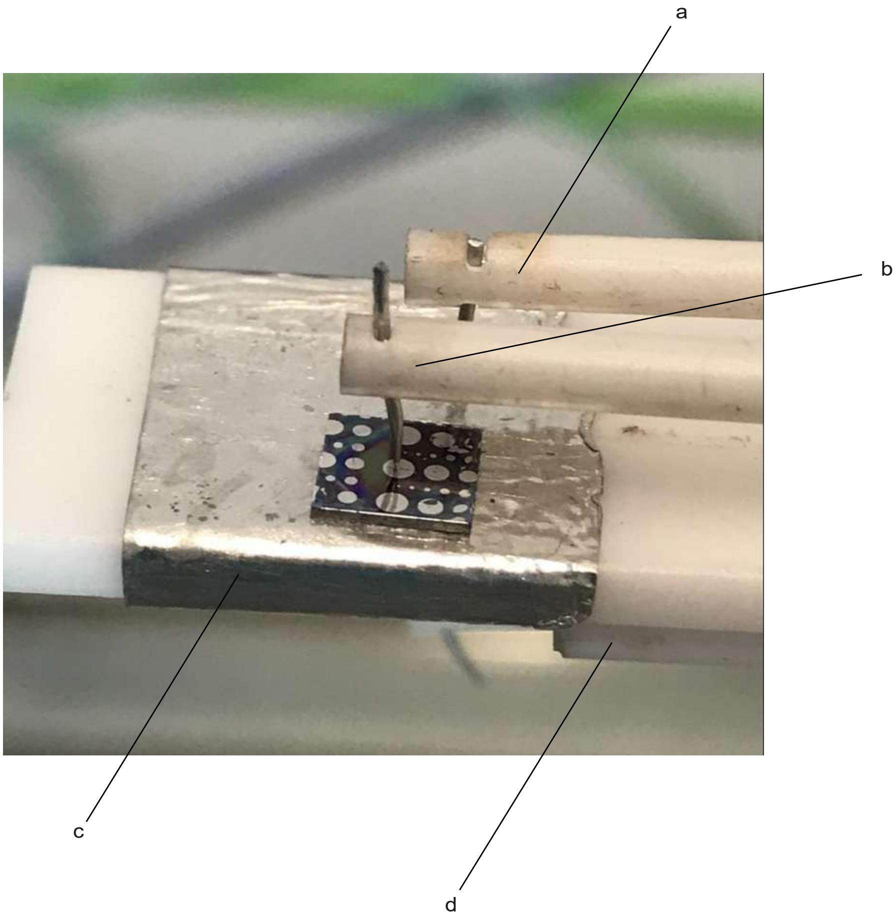

FIGURE 3.9: Photo of the measurement setup a) Needle connect to the counter electrode b) Needle connected to the microelectrode (approximately 700 µm) on the working electrode (STO) c) Pt-sheet on the sample holder for the connection of the counter electrode d) Thermocouple

Half cell battery

Electrical measurements of the half cell battery carried out in a setup similar to the previous one, utilizing a tube furnace uniformly heated at a temperature of 500, (±5),° C, that was monitored by a Type-K thermocouple positioned 1 cm below the sample holder in 1% bar O_2. Note that the gas flow bubbled through the setup prior to the electrical measurement.

Pt-Ir needles were affixed to the working electrode and the counter electrode was connected with the needle with the use of the Pt wire (refer to Figure 3.10 for additional details).

Galvanostatic cycling with potential limitation (GCPL) was executed using a Keithley 2600 source meter in a 2-wire configuration, employing DC currents ranging from 8 to 20 µA. Direct currents were applied between the counter and the working electrode, while voltages were recorded between the working and reference electrode.

10 cycles were measured between 0 V (low) and upper cut-off voltage between 1.5 to 2 V. The potential versus 1 bar oxygen were calculated with Nernst's Equation (3.4).

$$U_{vs1barO_2} = U_{vs1\%O_2} - \frac{RT}{4F} \exp \frac{1bar(O_2)}{0.01bar(O_2)} \tag{3.4}$$

where $U_{vs1\%O_2}$ is the measured voltage and $U_{vs1barO_2}$ is voltage against 1 bar O_2.

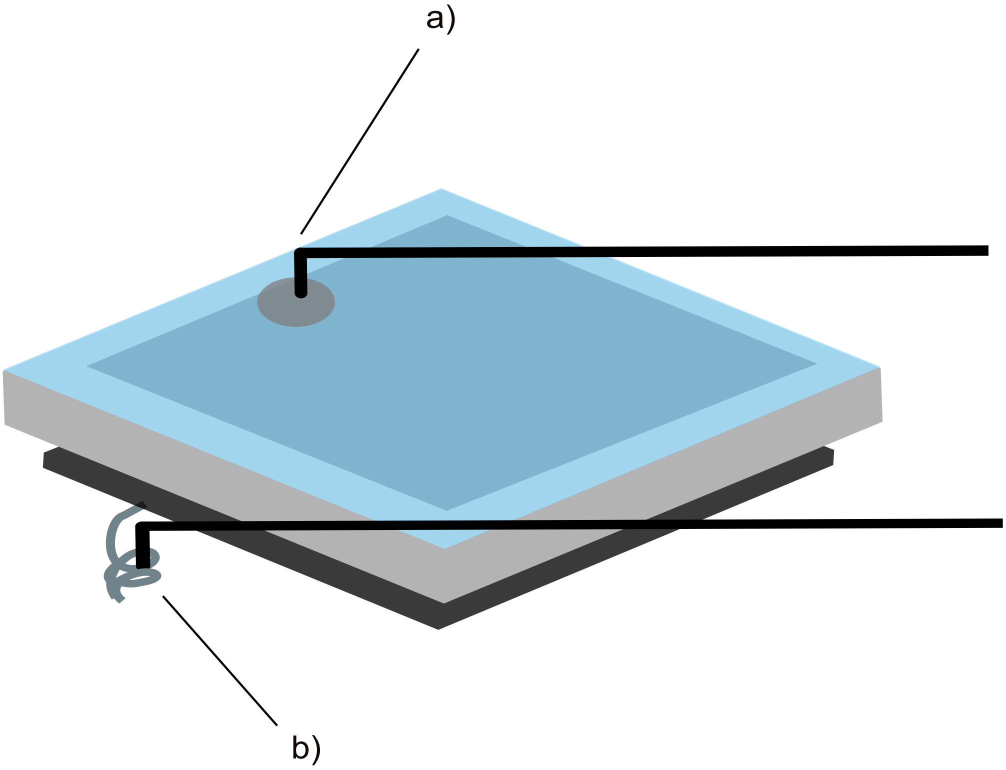

FIGURE 3.10: Schematic illustration of the battery half cell connection with the needle a) working electrode connected directly with a needle on the brushed Pt on top of the Ti/Pt sputtered layer (working electrode is covered by Ti/Pt sputtered layer and sealed with a glass layer to prevent the oxygen uptake of the atmosphere except a very small point which used for the electrical connection) b) counter electrode connected to the needle via a Pt wire, that was attached on the back side of the (LSF/Pt) counter electrode by Pt paste

4 Results and Discussion

4.1 Analytical characterization of STO thin films

4.1.1 Exploration of the effect of the annealing temperature on STO thin film

The influence of annealing temperature on the morphological and structural alterations of materials is well-established. However, our study focuses specifically on examining the impact of annealing temperature variations on the structure, surface morphology, and stoichiometry of sol-gel prepared STO thin films.

GIXRD

Figure 4.1 shows diffractograms of STO thin films annealed at 550 °C, 650 °C, 750 °C and 850 °C for 3 hours. The high energy of X-rays enables deep penetration into the sample, potentially revealing the distinctive characteristics of YSZ and the STO thin films. Ensuring that the diffracted beam originates from the thin film layer is crucial. Utilizing GIXRD measurement, where the low incident beam angle can only penetrate through the STO thin films, becomes the preferred technique for this purpose. While this approach offers the advantage of shallower penetration, it may also result in lower intensity of reflections. The diffractogram taken for a STO thin film annealed at 550 °C (dark teal in Figure 4.1) shows reflexes similar to the amorphous material. Whereas, by increasing the annealing temperature of the STO thin films to 650 °C, 750 °C and 850 °C, crystallization of the STO thin films in the provskite structure can be observed. The three diffractograms belonging to 650 °C, 750 °C and 850 °C match the corresponding peaks found in the database for the perovskite type STO. Three highest intensity peaks at 32.3°, 46.33° and 57.63° indicate [110], [200], and [211] lattice planes, respectively, belong to the STO perovskite structure. All STO films annealed higher than 550 °C have a lattice parameter of $a = b = c = 3.9$Å. The sharpest reflexes were measured for STO thin films annealed at 850 °C (light blue diffractogram). Here, even reflexes with the smallest intensities, for example the [310], [311], and [222] reflexes at 77°, 82° and 86° 2θ, respectively, were clearly distinguishable, compared to the same reflexes for STO thin films with lower annealing temperatures. Based on those GIXRD results, an annealing temperature of 850 °C seems to provide the desired formation of the perovskite structure.

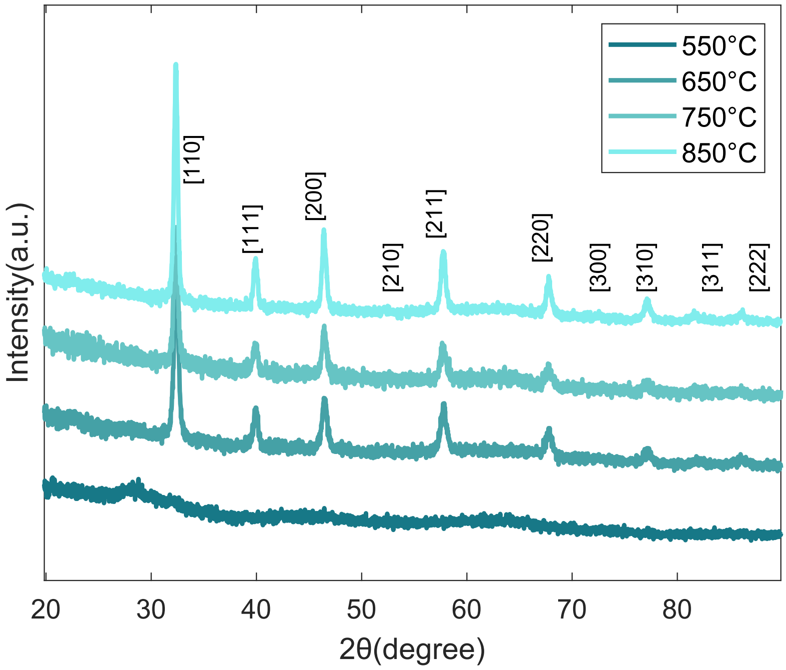

FIGURE 4.1: GIXRD of nominally identical STO thin films on YSZ single crystals annealed in a temperature range between 550 °C and 850 °C and a step size of 100 °C

SEM images

The surface morphology can be significantly impacted by the annealing temperature, influencing aspects such as surface roughness, grain size, and terrace-and-step structures.

Image (a) in Figure 4.2 presents the STO thin film annealed at 550 °C. As GIXRD confirmed previously, it exhibits an amorphous structure. The SEM image shows the presence of extra small grains. By increasing the annealing temperature, the morphology changes, as shown in image (b) in Figure 4.2, which represents the thin film annealed at 650 °C. This image illustrates particles on the surface, which may suggest variations in grain sizes, as indicated by GIXRD, without revealing any additional phases.

The STO film annealed at 750 °C shown in image (c) of Figure 4.2 exhibits fewer holes and cracks compared to the others, but it appears to have a rough surface.

Image (d) in Figure 4.2 corresponds to the thin film annealed at 850 °C, which shows somewhat condensed layer but with cracks on the surface.

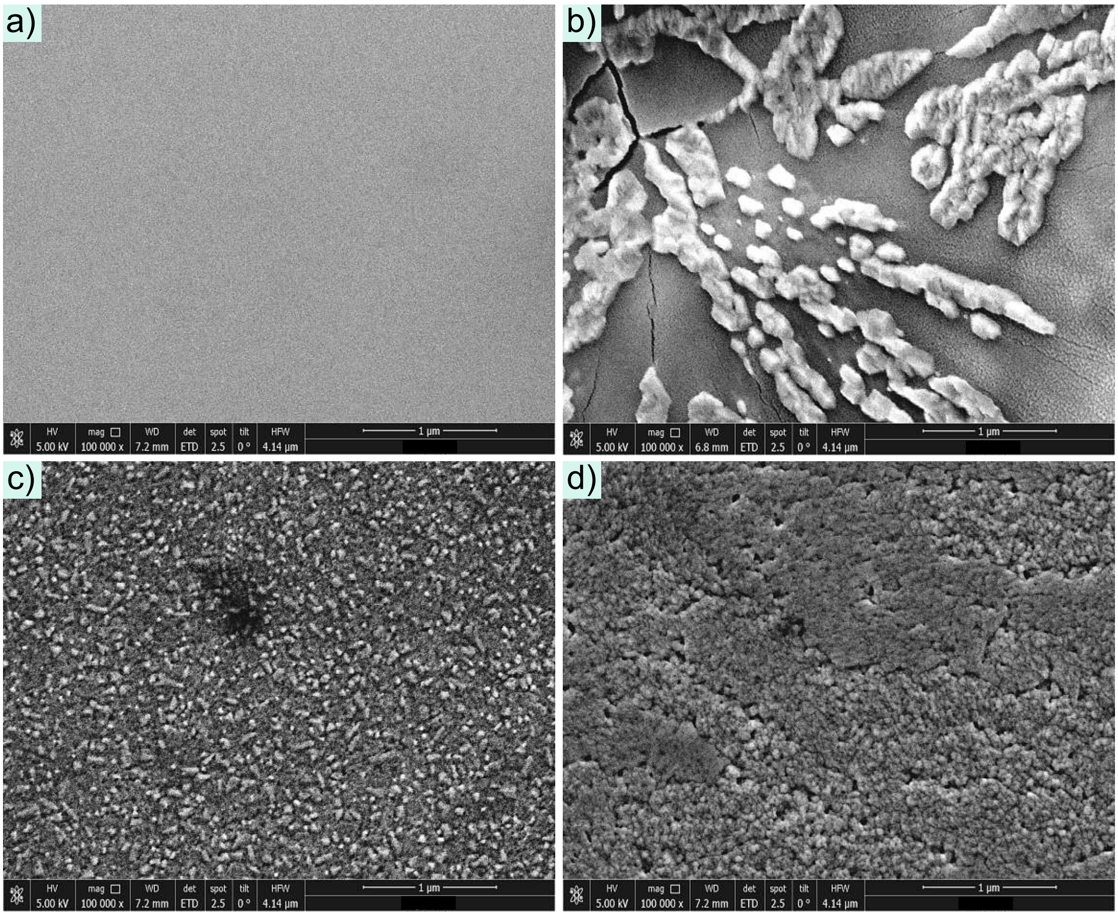

FIGURE 4.2: SEM images of STO thin films grown on YSZ single crystals at annealing temperatures of a) 550 °C b) 650 °C c) 750 °C and d) 850 °C

The STO thin film annealed at 850 °C exhibited satisfactory results in both GIXRD analysis and surface morphology. To further investigate the morphologies of the cross-section layer, a cross-sectional SEM image was captured. As depicted in Figure 4.3, this image reveals a partially compact layer characterized by cylindrical shapes.

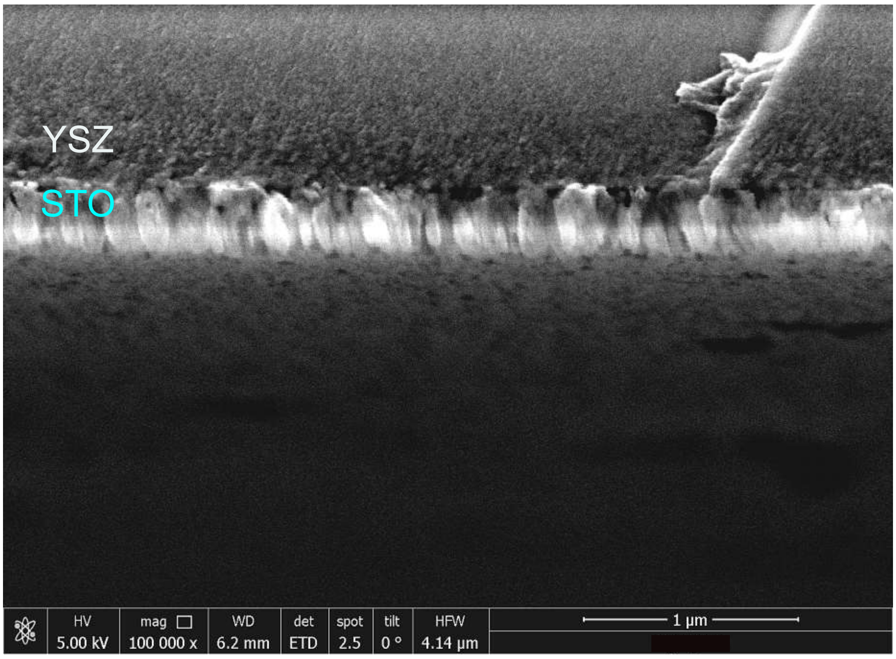

Figure 4.3: Cross-section SEM image of the STO thin film annealed at 850 °C

LA-ICP-MS

LA-ICP-MS measurements were initially employed to determine the stoichiometry of STO thin films prepared via the sol-gel process. To ensure complete ablation of the entire thin film, mass spectroscopy was used to measure the presence of yttrium and zirconium elements in the YSZ single crystal substrate. Five repetitive of a laser line were utilized for an ablation. The first laser pulse targeted approximately two-thirds of the thin film layer, while the second reached deeper into YSZ. Figure 4.4 shows that the STO layer was ablated by the first pulse, however neither yttrium nor zirconium were measured. Repetitive ablation of the second scan line shows that both yttrium and zirconium were ablated, indicating almost complete removal of the STO thin film.

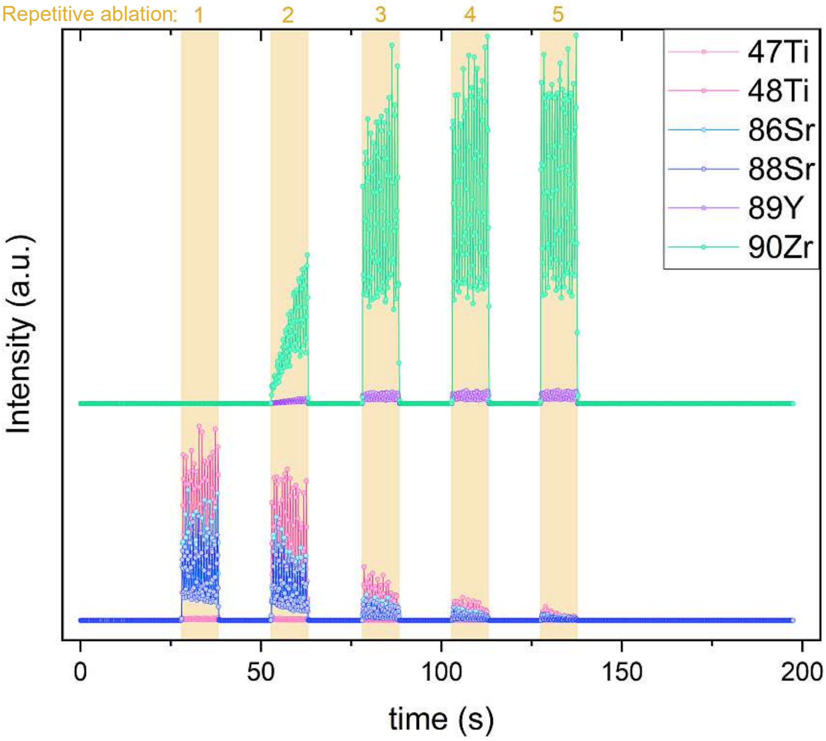

FIGURE 4.4: Five repetitive ablation of a scan line, showing that the STO thin film is almost fully ablated after second repetition

In preceding sections, we explored the impact of annealing temperature on the surface morphologies of thin films and the presence of the perovskite structure. Additionally, it is important to consider that variations in annealing temperatures can also affect the stoichiometry of the thin film layers. As shows in Table 4.1, all thin films annealed within the temperature range of 550 °C-850 °C exhibit Sr depletion to some extent. Specifically, the thin film annealed at 550 °C displays the highest concentration of Sr vacancies, while raising the annealing temperature leads to a decrease, with Sr vacancies stabilizing at approximately 20%.

Furthermore, it is notable that in Subsection 4.1.1, thin films annealed at temperatures higher than 550 °C exhibit diffractograms of pure perovskite materials. While the GIXRD method is capable of detecting the structure of the material, it may not be sensitive enough to detect low concentrations of vacancies that do not significantly influence the perovskite structure. However, indirect indicators of vacancies, such as lattice parameter deviations, might still be observable in GIXRD data. But in a previous section, the lattice parameters of the crystals were perfectly matched to a perovskite structure. Nevertheless, LA-ICP-MS analysis reveals a 20% vacancy concentration. This observation suggests that perhaps the single-point calibration by the use of the single crystal may have been insufficient, potentially leading to discrepant findings in the results. Therefore, for the sake of the clarity, LA-ICP-MS measurements should be repeated using different calibration reference.

TABLE 4.1: Stoichiometry of STO thins film annealed at 550 °C, 650 °C, 750 °C and 850 °C

STO thin film annealed at 550 °C	$Sr_{0.66}Ti_1O_3$
STO thin film annealed at 650 °C	$Sr_{0.75}Ti_1O_3$
STO thin film annealed at 750 °C	$Sr_{0.81}Ti_1O_3$
STO thin film annealed at 850 °C	$Sr_{0.80}Ti_1O_3$

Atomic Force Microscopy (AFM)

Selected samples underwent scanning with AFM to investigate surface roughness characteristics. As discussed in the previous section, SEM images provided insight into the surface morphologies. Specifically, Subsection 4.1.1 demonstrated that surface morphology can be influenced by the annealing temperature. In Figure 4.5, image (a) and (b) depict STO thin films grown on YSZ, that were annealed at 750 °C and 850 °C, respectively. It is evident that the surface of the STO thin film annealed at 850 °C (Figure 4.5 b) is denser compared to Figure 4.5 a), the STO thin film annealed at 750 °C. However, Figure 4.5 b) also reveals the presence of cracks in the STO thin film.

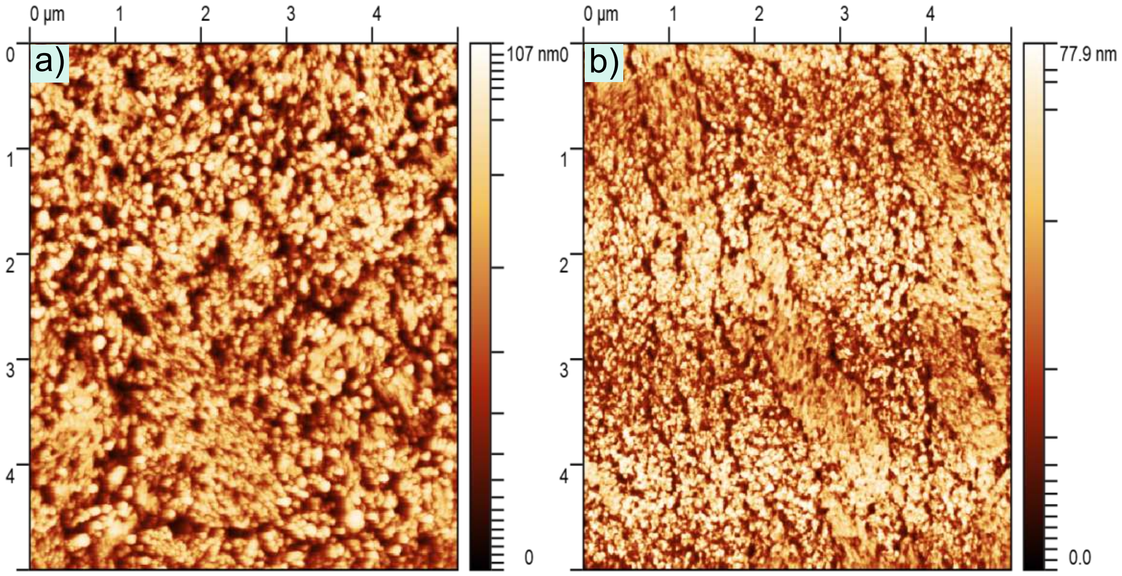

Figure 4.5: AFM scan of STO thin films on YSZ single crystals, a) STO annealed at 750 °C b) STO annealed at 850 °C

The RMS roughness (Root Mean Square) were calculated for each sample. RMS is a statistical measure used to assess surface roughness or smoothness. RMS is determined by taking the square root of the mean of the valleys and peaks from the mean line within a specified evaluation area.

The RMS values calculated for the STO thin film annealed at 750 °C (Figure 4.5 a) and 850 °C (Figure 4.5 b) were 9.8 nm and 5.8 nm, respectively. These calculations indicate that the STO thin film annealed at 850 °C exhibits a smoother surface compared to the one annealed at 750 °C. Figure 4.6 shows 2D line scans across 5 µm of STO thin films annealed at 750 °C and 850 °C, and indicates difference in surface roughness.

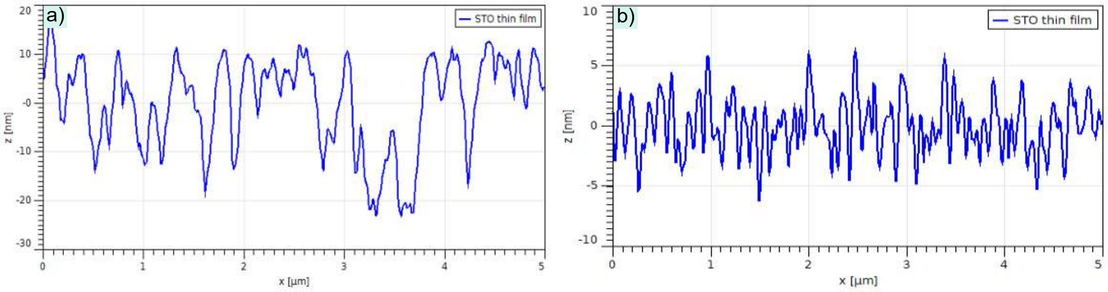

Figure 4.6: 2D line scan of STO thin films on YSZ single crystals, a) STO annealed at 750 °C b) STO annealed at 850 °C

4.1.2 Precursor aging time

In the sol-gel process, it is known that the duration of the precursor aging could impact the porosity of the resulting material. To eliminate the influence of the aging precursor on the STO thin films, nominally identical STO thin films were deposited using the same precursor over a period of three months.

GIXRD

Figure 4.7 presents diffractograms of three nominally identical STO thin films, each annealed at 850 °C with the same precursor aged for 48 hours, one month, and three months, respectively. While the diffractogram of the STO film with a three months old precursor exhibits lower intensity compared to the others, this variance could potentially stem from sample size differences. However, it is evident that all three precursors, despite their varying ages, crystallize into the perovskite structure.

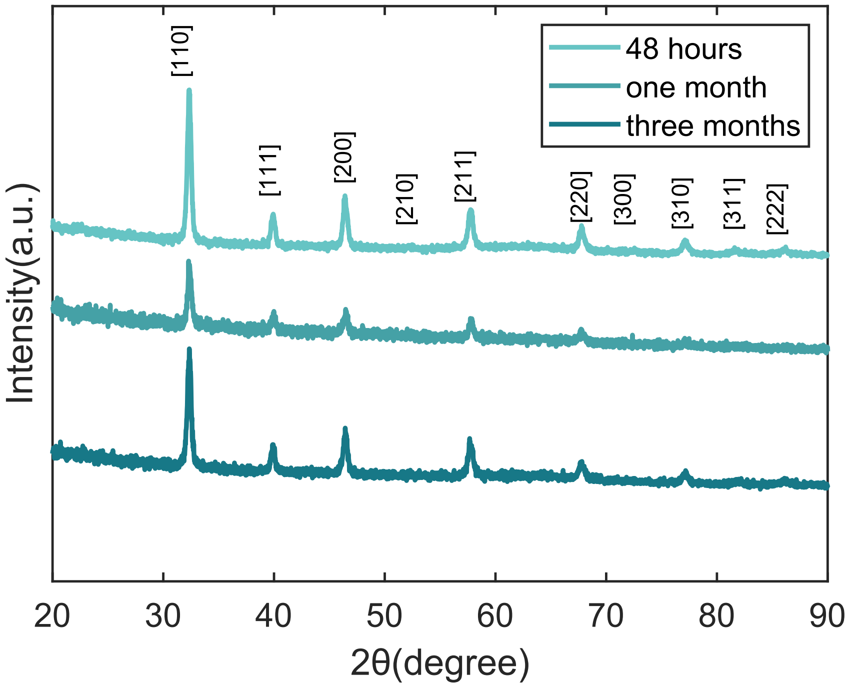

FIGURE 4.7: GIXRD of nominally identical STO thin films on YSZ single crystals prepared with a precursor that has been aged for 48 hours, one and three months (annealed at 850 °C)

SEM images

SEM images of three nominally identical STO thin films are shown in Figure 4.8. In all three SEM images, it is evident that the surface is partially compact, but in some extent exhibits cracks and holes. Furthermore, the grain sizes are clearly visible in image a) of Figure 4.7, but appear smaller in image b), and become increasingly difficult to distinguish in image c).
Based on these images, it is evident that the morphologies of the surface can be influenced by the precursor aging time, while the perovskite structure remains consistent across all nominally identical STO thin films, as confirmed by GIXRD analysis.

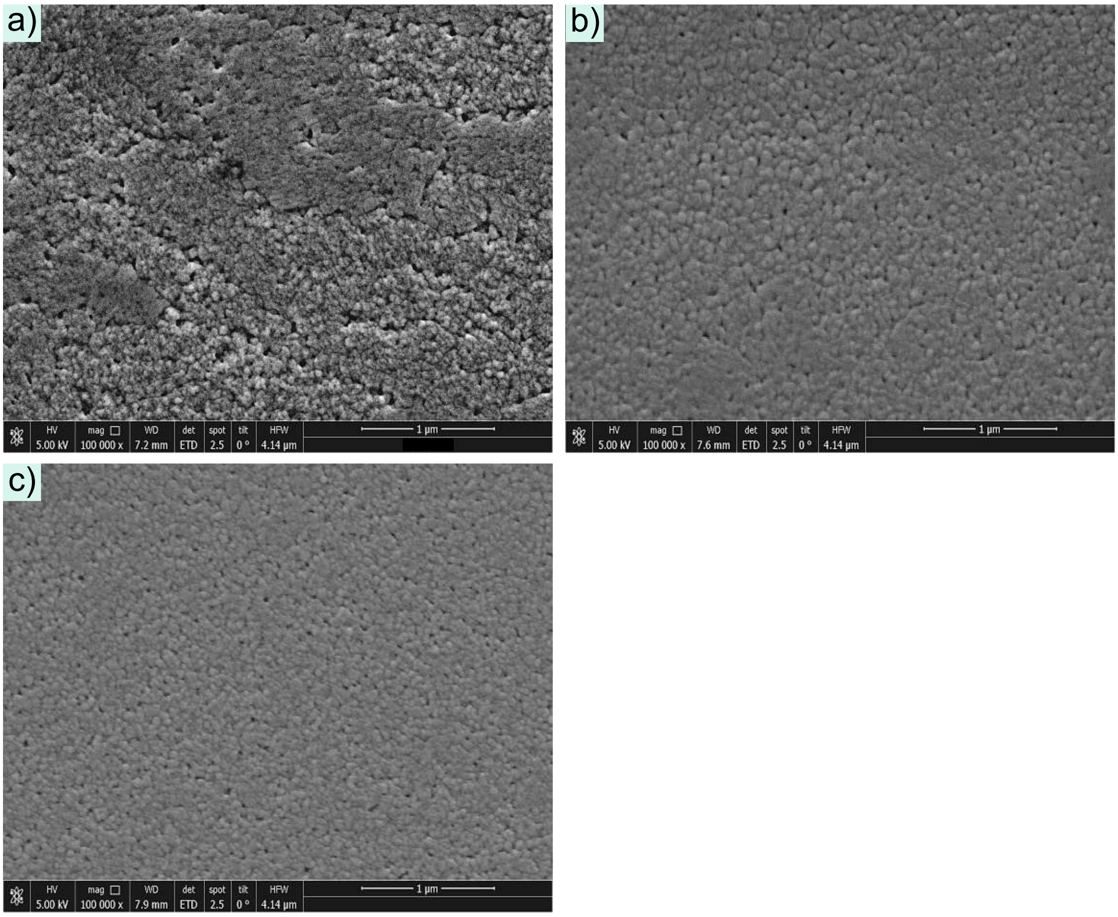

FIGURE 4.8: SEM image of three nominally identical STO thin films grown on YSZ single crystal using the same precursor with an aging duration of 48 hours, b) one month and c) three months.

LA-ICP-MS

The LA-ICP-MS method was employed to investigate the stoichiometry of two nominally identical STO thin films grown on YSZ using the same precursor with aging durations of 48 hours and three months. The analysis revealed that Sr vacancies were present in both samples. The precursor aged for 48 hours has a stoichiometry of $Sr_{0.93}Ti_1O_3$, whereas the precursor aged for three months shows more Sr vacancies, with a stoichiometry of $Sr_{0.89}Ti_1O_3$. Although the difference is minimal, it may have arisen from the calibration used for these measurements.

Table 4.2: Stoichiometry of two nominally identical STO thin films grown on YSZ single crystal using the same precursor with an aging duration of 48 hours and three months

Precursor after 48h	$Sr_{0.93}Ti_1O_3$
Precursor after three months	$Sr_{0.89}Ti_1O_3$

4.1.3 Variations of the Sr to Ti ratio in the precursor

Sr vacancies can indeed influence the electrochemical properties of STO thin films. As demonstrated in previous sections, each STO thin film sample exhibited a certain amount of Sr depletion. To investigate this phenomenon further, the amount of Sr was doubled and halved to assess whether Sr content could be precisely controlled. Additionally, the effect of the Sr:Ti ratio variation on the morphology and the perovskite structure was investigated.

GIXRD

The diffractogram of prepared precursors with Sr:Ti ratios of 0.5:1, 1:1, and 2:1 is illustrated in Figure 4.9. GIXRD analysis reveals that the sample with a 0.5:1 ratio of Sr:Ti exhibits an amorphous structure with some degree of crystallization. Two low-intensity peaks at 32° and 46° correspond to the [110] and [200] lattice planes of STO perovskite, respectively.

The sample with a 1:1 Sr:Ti ratio exhibits a perovskite structure similar to previous investigations, displaying all peaks associated with the perovskite structure except for the last three, with small intensity, observed and showing at 77°, 82°, and 86° the [310], [311], and [222] reflexes, respectively.

The sample with a 2:1 Sr:Ti ratio exhibits a Ruddlesden-Popper-type perovskite structure with the generall formula $A_{n+1}B_nO_{3n+1}$, where A and B are cation and O is oxygen or anion and n represents the count of octahedral layers within the Ruddlesden-Popper-type perovskite arrangement [49]. In this structure, the perovskite layers are sandwiched with thermodynamically stable rock salt layers of SrO, owing to the excess amount of Sr present in the material [50].

A STO thin film grown on YSZ with a 2:1 Sr:Ti ratio has a formula of $Sr_2Ti_1O_4$ with n=1. GIXRD analysis of this material reveals diffraction peaks corresponding to the STO perovskite structure, as well as additional peaks at 31° and 46°, which represent the lattice planes of SrO. The lattice parameters for this structure are $a = b = 3.88$ Å and $c = 12.59$ Å.

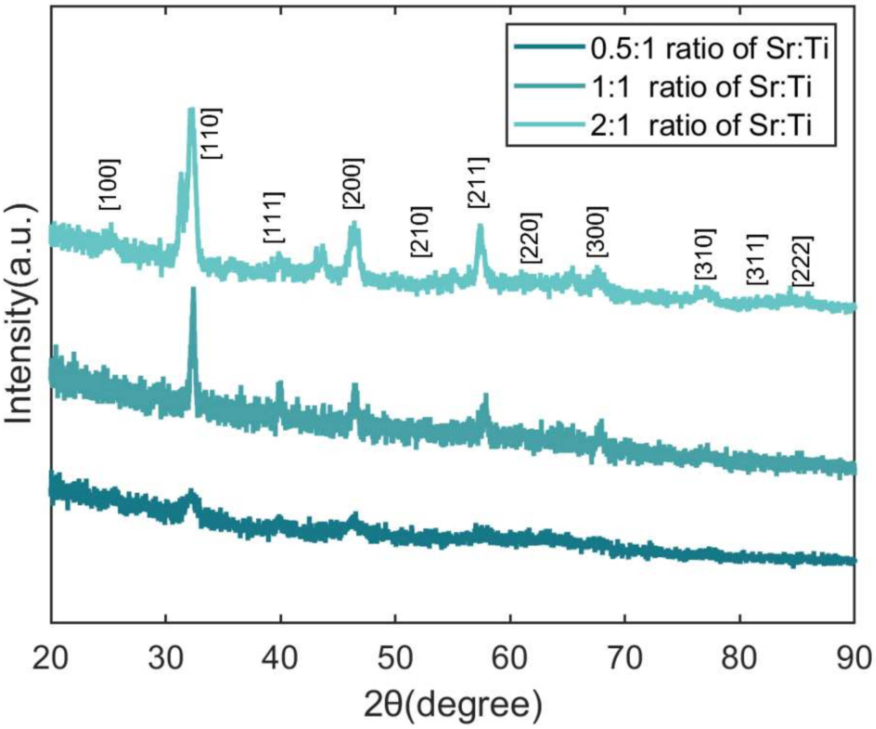

FIGURE 4.9: GIXRD of STO thin films with a Sr.Ti ratio of 0.5:1, 1:1 and 2:1 in prepared precursors.

SEM images

Figure 4.10 presents SEM images of samples with variations in the Sr:Ti ratio. These images demonstrate the impact of altering these elements on the surface morphologies. This finding demonstrates the importance of understanding the role of specific elements in shaping material characteristics morphology.

Figure 4.10 a) shows an STO thin film layer prepared with a 0.5:1 Sr:Ti ratio, as previously confirmed by GIXRD results indicating an amorphous layer, which is further supported by the SEM images showing an amorphous morphology.

Figure 4.10 b) depicts a 1:1 Sr:Ti ratio, which also illustrates more holes and grain boundaries compared to the previous sample annealed at 850 °C (see Figure 4.2 d).

The STO thin film with excess Sr (2:1 Sr:Ti ratio) is illustrated in Figure 4.10 c) This sample with excess Sr exhibits a Ruddlesden-Popper-type perovskite structure and shows big cracks on the surface, which may be attributed to the additional layer of SrO. Despite big cracks are presented on the surface of in this sample, it seems to exhibit a denser surface structure in compared to the one with a 1:1 Sr:Ti ratio. Although holes are present at the surface, they are smaller in size compared to the other sample, but they do exist.

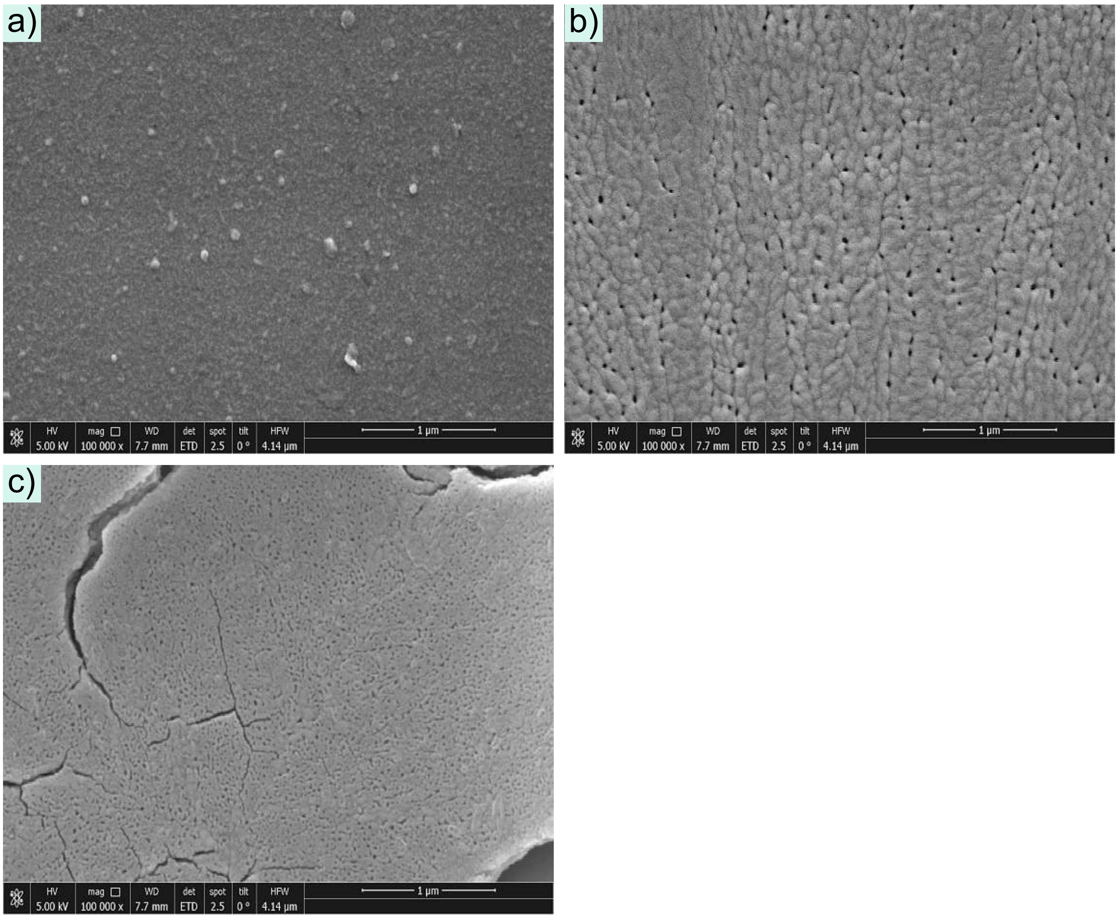

Figure 4.10: SEM images of STO thin films precursors with a Sr:Ti ratio of 0.5:1, 1:1 and 2:1 prepared with

LA-ICP-MS

The stoichiometry of STO thin films grown on YSZ with variation of Sr:Ti ratios in the precursor was measured using LA-ICP-MS. The findings indicate deficiency of Sr vacancies in all samples compared to the desired precursor stoichiometries. The sample with the 2:1 Sr:Ti ratio exhibiting the lowest Sr vacancies. Stoichiometric ratios were also found to be correlated with GIXRD and SEM results. For the sample with 0.5:1 Sr:Ti ratio, an amorphous structure with some crystallinity was observed, with LA-ICP-MS confirming the lowest Sr content in the structure, which could potentially result in an amorphous structure. Similarly, the 1:1 Sr:Ti ratio displayed approximately 10% Sr vacancies, consistent with previous findings for STO annealed at 850 °C. GIXRD analysis of the 2:1 Sr:Ti ratio suggested a Ruddlesden-Popper-type perovskite structure with a $Sr_2Ti_1O_4$ stoichiometry. This stoichiometry was almost confirmed by LA-ICP-MS, although oxygen content was not measured in this analysis.

Table 4.3: Stoichiometry of STO thin films grown on YSZ single crystals with variation of Sr:Ti ratio in the precursor

Precursor with 0.5:1 Sr:Ti ratio	$Sr_{0.45}Ti_1O_3$
Precursor with 1:1 Sr:Ti ratio	$Sr_{0.93}Ti_1O_3$
Precursor with 2:1 Sr:Ti ratio	$Sr_{1.9}Ti_1O_3$

4.1.4 Reproducibility of the sol-gel method

To validate the reproducibility of the sol-gel method for growing STO thin films on YSZ and assess its potential impact on the perovskite structure, morphology and stoichiometry, three nominally identical samples were analyzed and compared.

GIXRD

Figure 4.11 demonstrates that all three STO thin films exhibited identical perovskite structures. In all three diffractograms of the nominally identical STO thin films, peaks at angles of 32.4°, 46.4° and 57.7° with highest intensities correspond to the [110], [200], and [211] lattice planes of the STO perovskite structure. Additionally, peaks at angles of 40.3°, 67.8°, 81.8°, 86° and 57.6° correspond to the [111], [220], [310], [311], and [222] lattice planes, respectively. Peaks at angles of 52.3° and 72.7° (though barely visible) indicate the presence of the [210] and [300] lattice planes. The lattice parameters of all three nominally identical STO thin films were determined to be $a = b = c = 3.9$ Å.

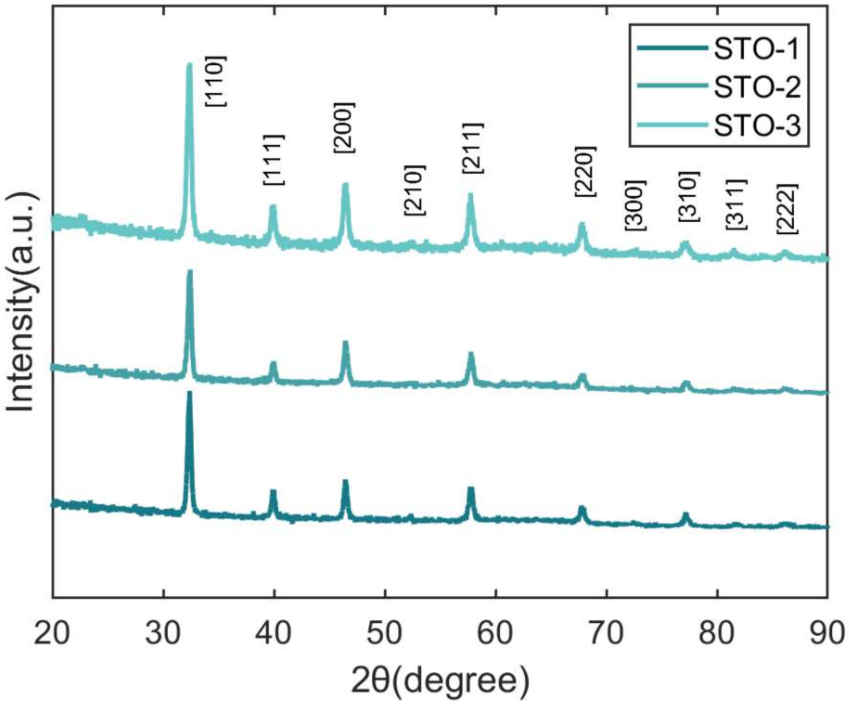

Figure 4.11: GIXRD of three nominally identical STO thin films grown on YSZ single crystals

SEM images

The morphologies of STO thin films grown on YSZ can affect the electrochemical properties of these films. As depicted in Figure 4.12, SEM images illustrate the characteristics of three nominally identical STO thin films grown on YSZ. While the overall morphology appears consistent, with all films exhibiting holes and cracks across the surface, there is a noticeable variability in the thin film surface density. In particular, SEM image (a) in Figure 4.12 reveals larger holes compared to SEM images (b) and (c). Moreover, SEM images (a) and (b) suggest a larger grain size in comparison to (c).

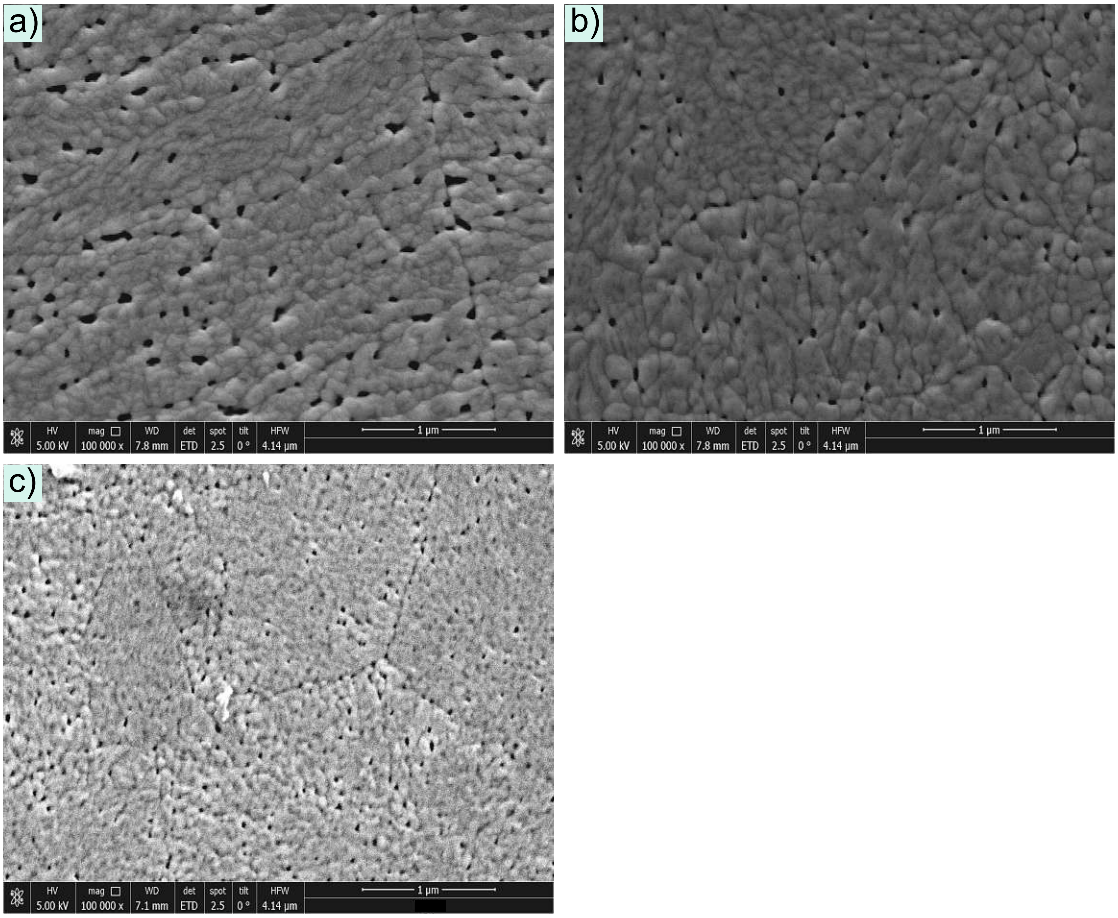

Figure 4.12: SEM images of nominally identical STO thin films grown on YSZ single crystal, a) STO-1 b) STO-2 c) STO-3

LA-ICP-MS

The stoichiometric reproducibility of STO in nominally identical thin films grown on YSZ is demonstrated in Table 4.4. Despite the existence of Sr vacancies and slight differences between STO-1, STO-2, and STO-3, the stoichiometry remains reproducible.

Table 4.4: Stoichiometry results of three nominal identical STO thin films grown on YSZ

STO-1	$Sr_{0.97}Ti_1O_3$
STO-2	$Sr_{0.95}Ti_1O_3$
STO-3	$Sr_{0.95}Ti_1O_3$

Atomic Force Microscopy (AFM)

Figure 4.13 depicts the AFM images of nominally identical STO thin films grown on YSZ for investigating the reproducibility of the STO thin films prepared via the sol-gel method. As discussed in Subsection 4.1.4, the morphology of the surface is not certainly reproducible using the sol-gel method. Additionally, Figure 4.13 illustrates that the topology of two nominally identical STO thin films differs within a 5×5 µm^2 area.
In detail, Figure 4.13 (a) displays larger grain sizes and some denser regions, alongside areas with holes. On the other hand, Figure 4.13 (b) reveals a surface with smaller grain sizes compared to Figure 4.13 (a), along with additional visible cracks observed also in the SEM images.

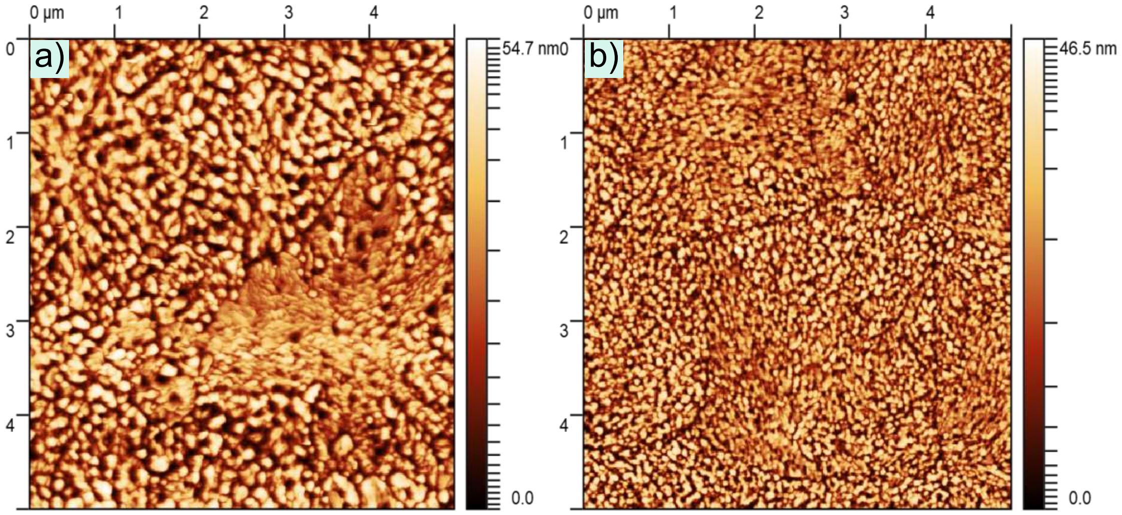

Figure 4.13: AFM scan of STO thin films on YSZ single crystals, a) STO-2 b) STO-3

Figure 4.14 shows the 2D line scan of those nominally identical STO thin films, where the differences in surface roughness can be seen. The RMS calculations reveal a roughness of 6.3 nm and 3.6 nm for STO-2 and STO-3, respectively. This further confirms that two nominally identical STO thin films exhibit distinct roughness properties, with STO-3 exhibiting a smoother surface compared to STO-2. Such differences could arise from non-homogeneous growth of the STO thin film on YSZ.

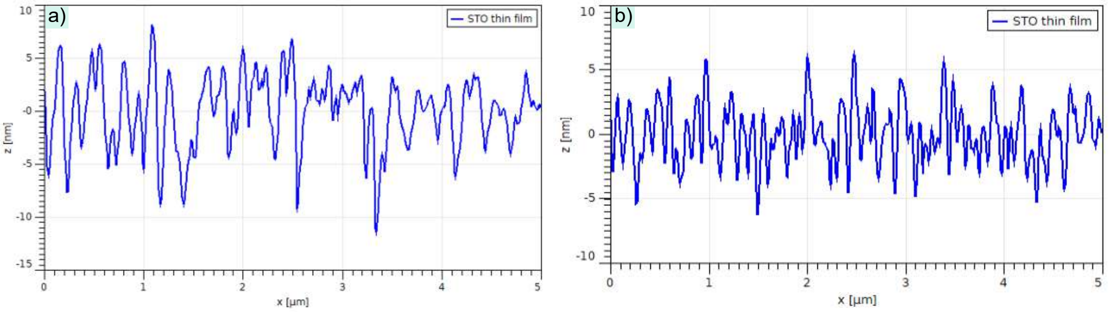

FIGURE 4.14: 2D line scan of STO thin films on YSZ single crystals, a) STO-2 b) STO-3

4.2 Electrochemical characterization of STO thin films prepared by sol-gel process

Electrochemical characterization of STO investigates the electrochemical behavior of STO thin films prepared via the sol-gel method by using EIS and galvanostatic cycling. We measured the chemical capacity under bias conditions and calculated the oxygen vacancies concentration. Additionally, we evaluated the STO conductivity using EIS, where we focused on samples grown on Nb:STO substrates. Furthermore, we validated STO's potential as an ion exchange battery through galvanostatic cycling on YSZ substrates. By employing these techniques, we gained valuable insights into optimizing STO thin films for various electrochemical applications.

4.2.1 Impedance measurements of STO sol-gel thin films under applied bias voltage

Impedance measurements of the produced STO sol-gel thin films were performed at 500 °C using a novel setup, where the STO thin films served as kind of working electrodes on YSZ single crystal substrates. The use of GDC/FeO as counter electrodes allowed control of the oxygen non-stoichometry through the application of a bias voltage in the range of -1 to +1V vs. Fe/FeO, equalling to an oxygen partial pressure range of 10^{-3} bar down to 10^{-55} bar. EIS experiments were carried out with potential steps of 10 mV. Figure 4.15 illustrates impedance diagrams, that were obtained within the voltage ranges of 0 V to 1 V and 0 V to -1 V vs. Fe/FeO. Increasing the voltage from 0 to 1 V vs. Fe/FeO leads to the release of oxygen ions from the counter electrode into the STO, which serve as kind of the working electrode. This voltage range correlates to 10^{-29} to 10^{-3} bar oxygen partial pressure, respectively, thereby increasing the hole conductivity of the STO towards higher pO_2. The oxygen incorporation process into STO can be described by Equation (4.1):

$$\frac{1}{2}O_2 + V_O^{\bullet\bullet} \rightleftharpoons O^x + 2h^{\bullet} \tag{4.1}$$

Decreasing the voltage from 0 to -1 V vs. Fe/FeO causes a reduction in oxygen activity. This range of applied voltage represent 10^{-31} to 10^{-55} bar non-stoichiometry oxygen partial pressure, resulting in an increase in the oxygen vacancy and electron concentration in STO, thus enhancing the conductivity of the STO. The reaction for oxygen removal from STO can be described by Equation (4.2):

$$O_O^x \rightleftharpoons \frac{1}{2}O_2 + V_O^{\bullet\bullet} + e' \tag{4.2}$$

Figure 4.15 shows impedance spectra of an STO thin film on YSZ after applying voltage with the 10 mV range:

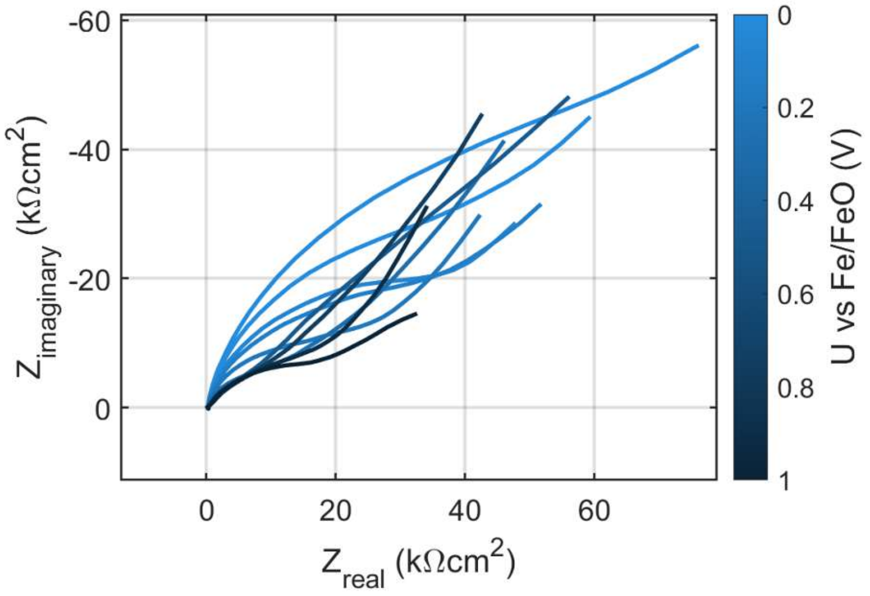

(a) Impedance spectra in the voltage range of 0 to 1 V versus Fe/Fe_2O_3 at 500 °C

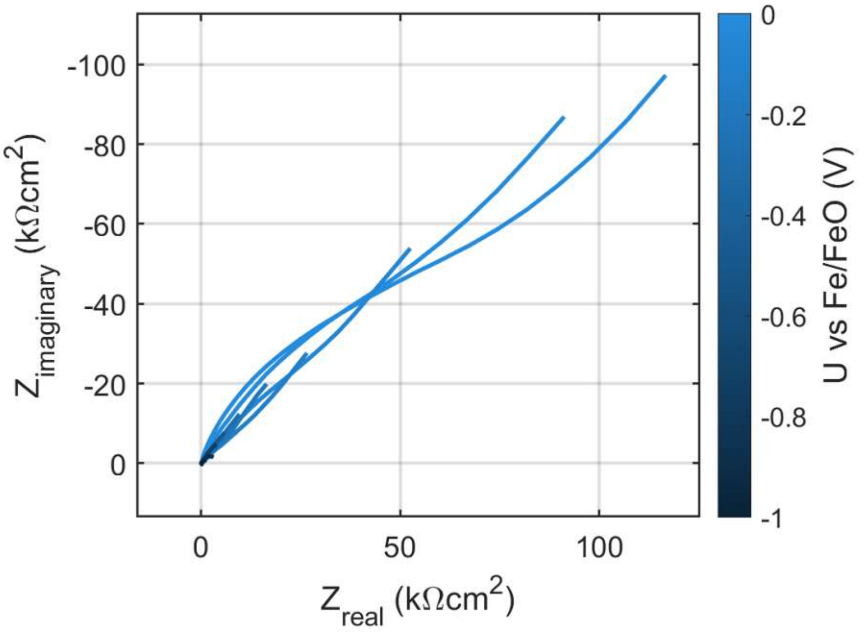

(b) Impedance spectra in the voltage range of 0 to −1 V at 500 °C

FIGURE 4.15: Impedance spectra of an STO thin film on YSZ with GDC/FeO as counter electrode

It's important to note that the voltage cannot be decreased indefinitely, as it can lead to electronic conductivity in YSZ, an effect known from Wagner-Hall measurements, as observed in Figure 4.16. The observed two semicircles (dark blue) correspond to the electronic conductivity of YSZ, this hindered continuation of our measurements to lower voltage [51].

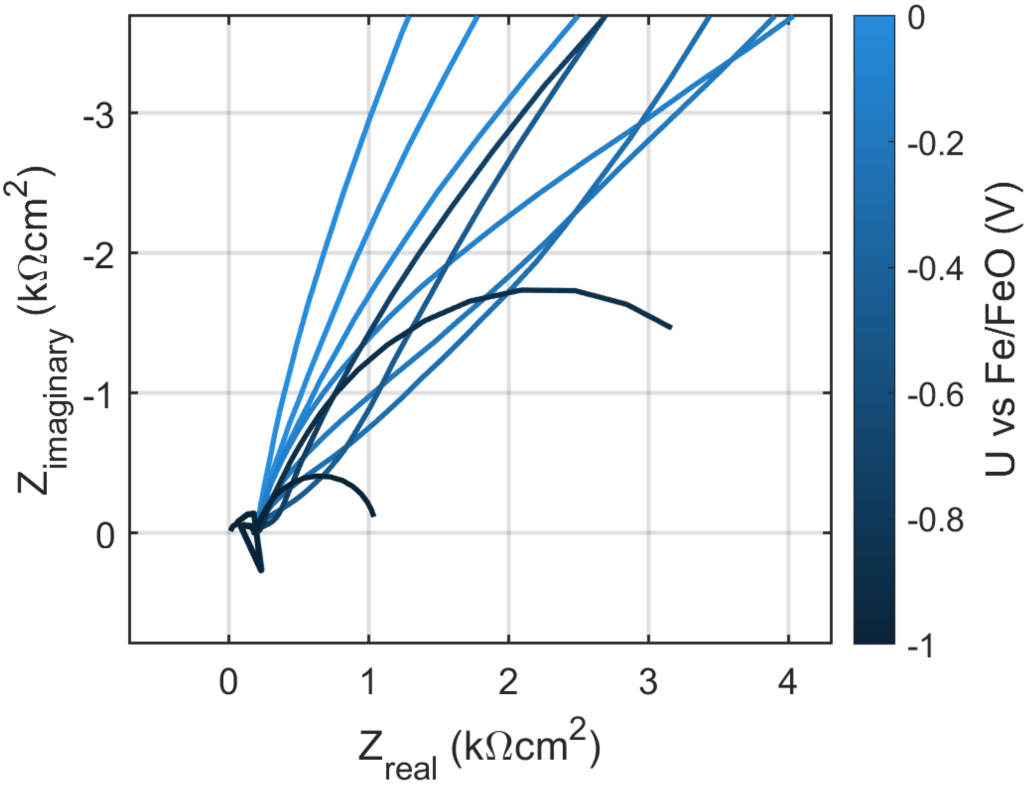

FIGURE 4.16: Closer look at the impedance spectra of STO thin film with a bias voltage of −0.9 to −1 V vs. Fe/FeO which shows Wagner-hall effect

Each impedance spectrum was analyzed by fitting it with four components representing different phenomena. The off-set of the impedance spectra in the high-frequency region was fitted by a *R* (resistor) describing the ionic conductivity of YSZ. In the mid-frequency range, the measured impedance spectra showed a semicircle with a shoulder. The main part of the semicircle was only described by a capacitance, which at very negative voltages continued to the capacitance part of the electronic conduction of YSZ. This shoulder of the semicircle is assigned as the STO bulk feature and was fitted using a parallel R-CPE-element, where the R element describes the total resistivity/conductivity (electronic and ionic) and CPE describes the chemical capacitance of the STO thin film. The rest of each impedance spectra remained unfit-

ted. Figure 4.17a illustrates an example of the measured impedance spectra, while Figure 4.17b displays the fitted part, along with the corresponding circuit model used for the fitting.
The term “chemical capacity,” denoted by the CPE element for STO, serves to fit the shoulder observed in impedance spectra at mid-frequencies. This element, represent a non-ideal capacitance behavior. The impedance of an CPE element can be described as given in Equation (4.3) [29, 44, 52]:

$$Z_{CPE} = Q^{-1}(j\omega)^{-n} \tag{4.3}$$

where n and Q are fit parameters, Q has capacitance information, n is the deviation from ideal semicircle which can be $0 \leq n \leq 1$ and ω is the angular frequency. Subsequently, the chemical capacitance can be calculated through Equation (4.4)

$$C_{Chem} = (R^{1-n} \times Q)^{1/n} \tag{4.4}$$

where R is the resistance of the STO thin film.

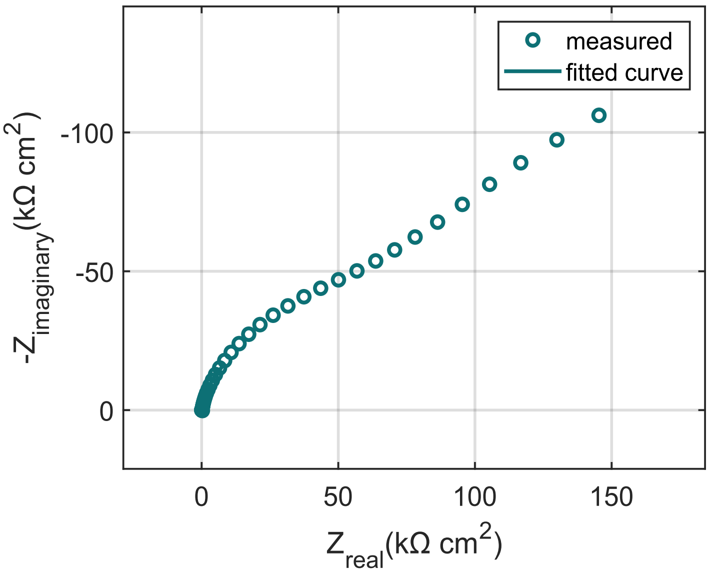

(a) Example of an impedance spectrum of a STO thin film measured without bias

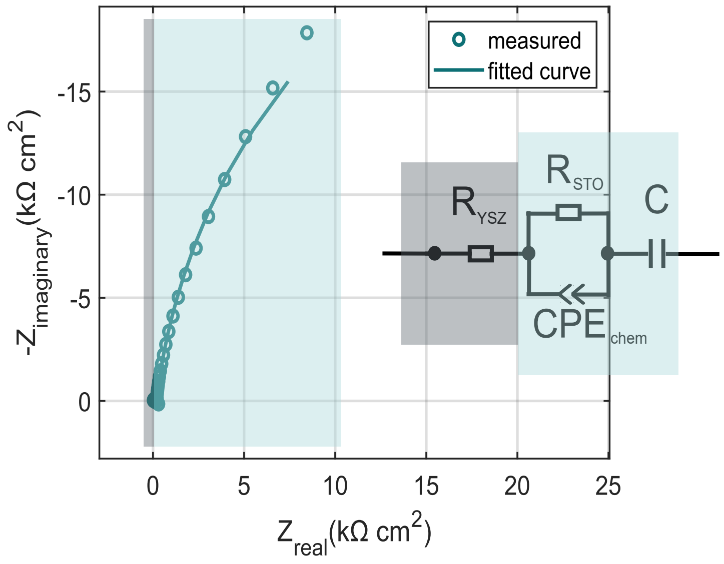

(b) Part of the impedance spectrum used for fitting with the shown circuit model. R_{YSZ} represent the ionic conductivity of YSZ, a parallel R-CPE-element is used for fitting the STO shoulder at mid-frequencies and a C element which is the electronic conductivity of the YSZ

Figure 4.17: Impedance spectra at the bias voltage and closer look at one of the impedance spectra of STO thin film on YSZ under bias with illustration of the fitting model

As shown in Equation (4.1) and Equation (4.2) variations in oxygen partial pressure can influence the electron charge carriers, primarily due to charge neutrality condition. The chemical capacitance can be effectively correlated with the defect chemistry of STO thin film through the volume-specific capacitance [29, 53]. Supposed we are in the non-stoichiometry regime described in Equation (4.2), then $c_{\text{V}} = \frac{1}{2}c_{eon}$:

$$C_{Chem} = \frac{e^2}{kT}\left(\frac{1}{4c_{\text{V}}} + \frac{1}{c_{eon}}\right)^{-1} \tag{4.5}$$

where c_{V} and c_{eon} represent the concentration of vacancies and electronic defects, respectively. e represents the elementary charge, and k represents Boltzmann's constant. Thus, the vacancy concentration can be calculated from C_{Chem}. Note that, the trapping effects are neglected here. The measured chemical capacitance were normalized by the thickness of the STO thin film, that was measured with SEM. Figure 4.18 shows a SEM cross-section of a STO thin film thickness with a layer of Ti/Pt sputtered on top as a current collector.

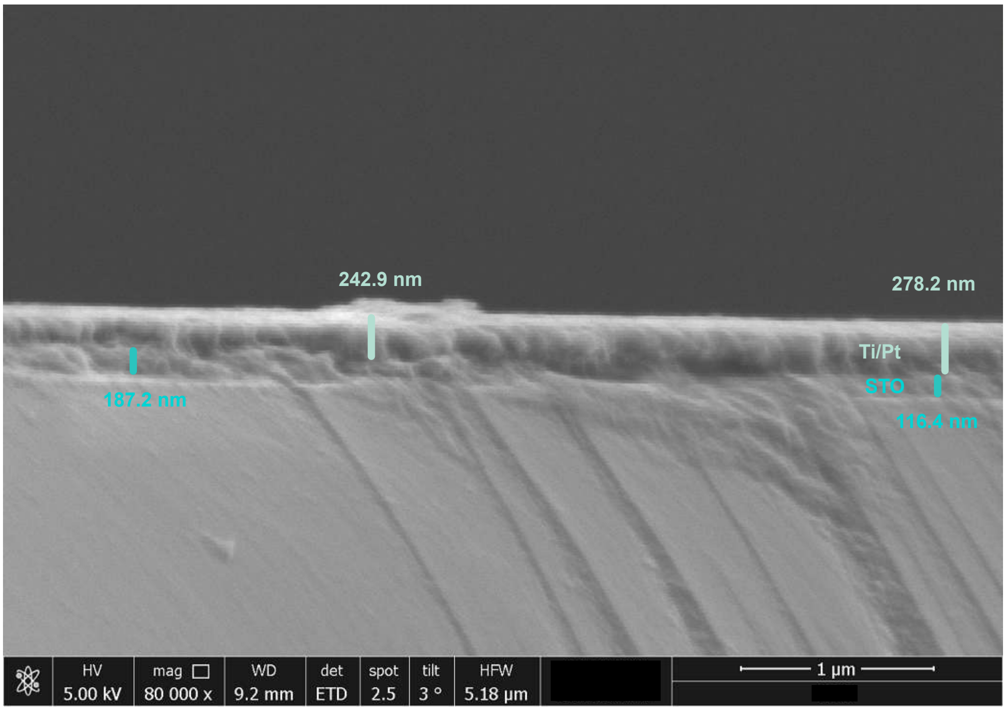

[redacted]

[redacted]

FIGURE 4.18: SEM image of a STO thin film with approximately 150 nm thickness on a YSZ single crystal. Ti/Pt layer were sputtered on top as a current collector with an approximately 260 nm thickness

The calculated oxygen vacancy concentration is plotted against the corresponding oxygen partial pressure in Figure 4.19. Our findings reveal a notable abundance of oxygen vacancies within the STO thin film, particularly evident at lower oxygen partial pressures in a range between 10^{-30} to 10^{-55} bar. This observation aligns excellently with the calculated Brouwer diagram of STO with 6 ppm Ti vacancies at 500 °C, please note that in the regime of intrinsic non-stoichiometry the exact (low) deficiency level is not relevant. (refer to Figure 4.20).

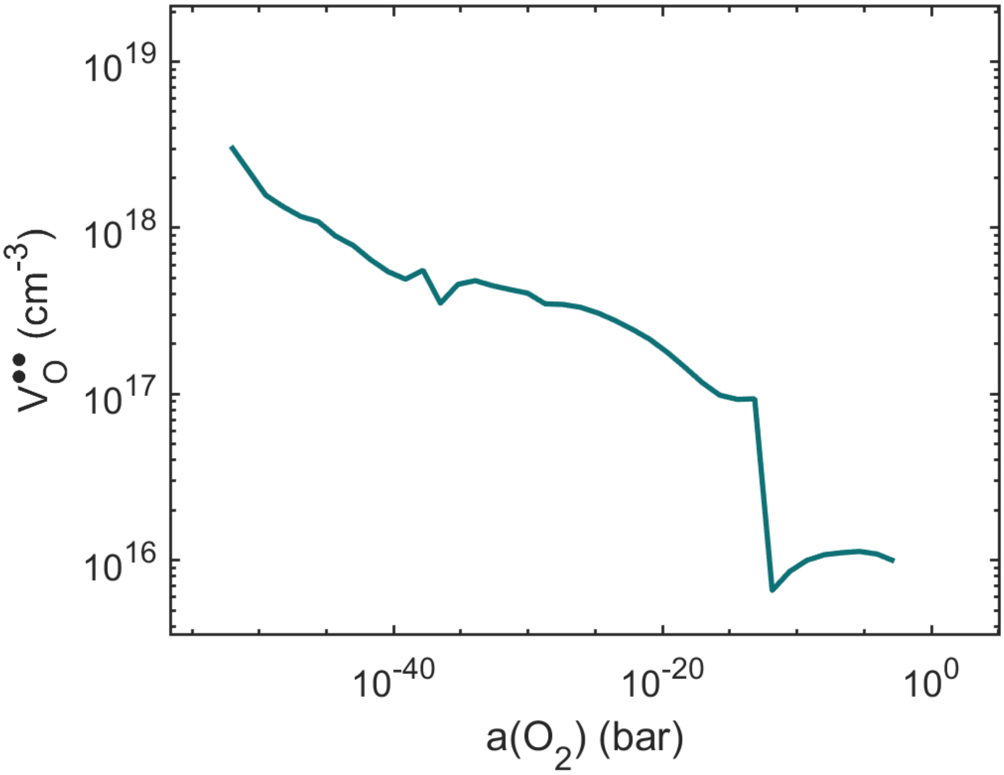

Figure 4.19: Defect concentration of oxygen vacancies in STO calculated from the chemical capacitance derived from impedance spectra at 500 °C, plotted against the oxygen partial pressure

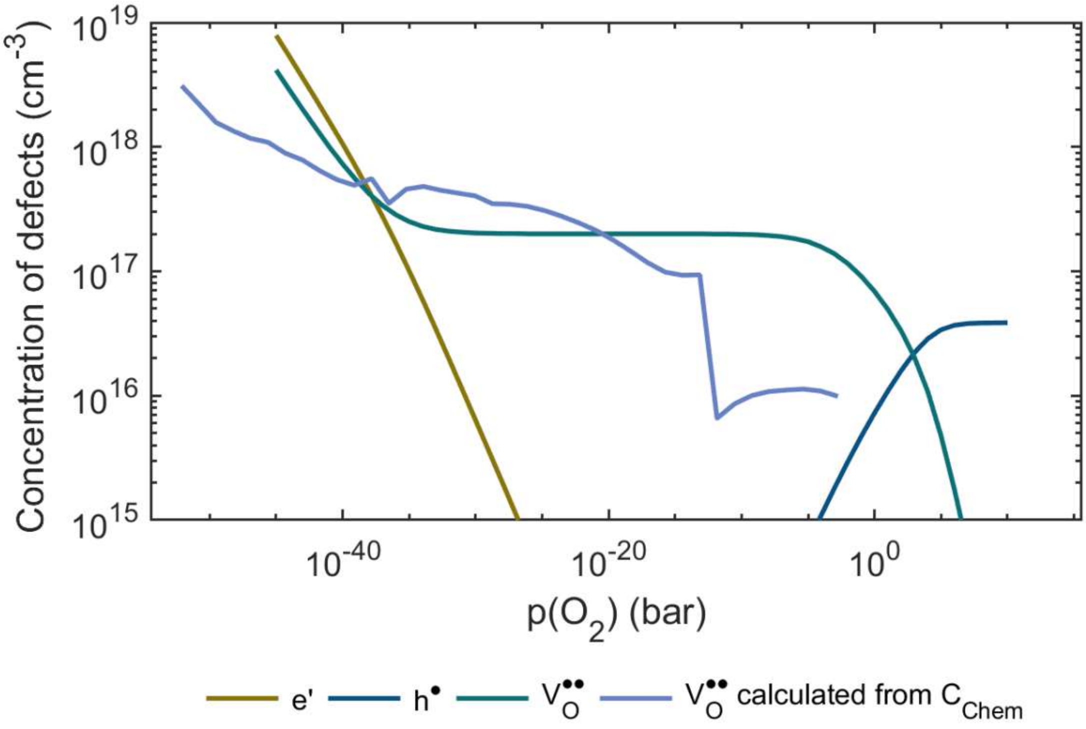

Figure 4.20: Brouwer diagram of STO at 500 °C with 6 ppm Ti vacancies and calculated oxygen vacancies from C_{Chem}

4.2.2 STO thin film on Nb:STO for conductivity measurement

The conductivity of the STO thin film, fabricated via the sol-gel process, was measured using impedance spectroscopy. STO is an ionic-electronic conductive material, in order to facilitate conductivity measurements, a Nb:STO single crystal served as the substrate. Notably, Nb:STO is characterized by its high electronic conductivity. This property is particularly advantageous as it can be blocking ion conduction, thereby enabling the measurement of electronic conductivity using EIS.

Impedance spectra of the STO film were obtained using microelectrodes sized 692 µm, 549 µm, and 413 µm, applied onto the STO layer. The measurements were conducted over a temperature range of 500 to 600 °C.

Figure 4.21 illustrates the impedance spectra obtained from EIS measurements using three different microelectrode sizes at 500 °C. Frequencies lower than 25 Hz and 31 Hz are considered as low frequencies. Notably, at the lowest frequencies, a distinct behavior is observed, characterized by an x-axis intersection ($\omega \rightarrow 0$), which corresponds to the parameter R_{DC}. This intercept is attributed to the blocking of ion conductivity at both side of the STO. R_{DC} represents, therefore, the electronic resistance of the STO thin film.

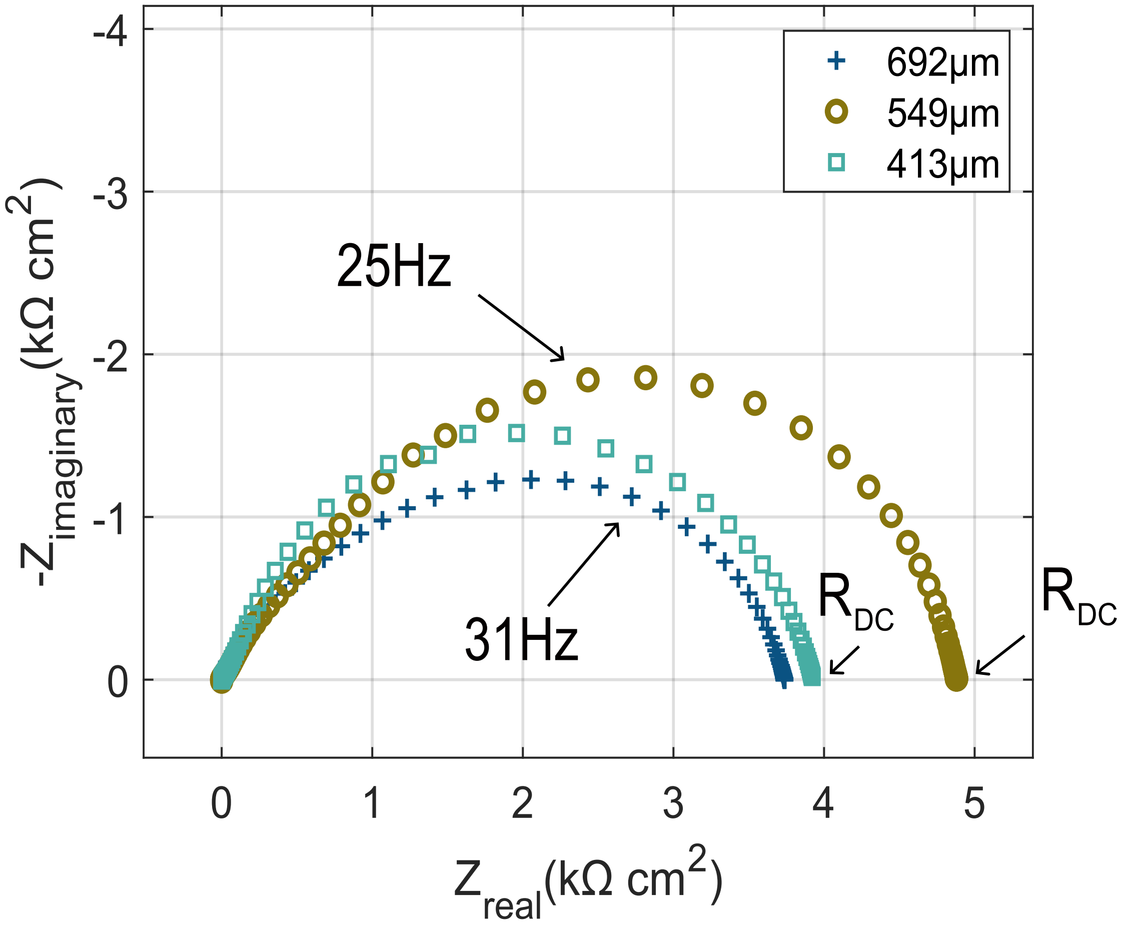

FIGURE 4.21: Impedance spectra of an STO thin film measured with microelectrodes of different sizes at 500 °C.

Figure 4.22 provides an illustrative representation of the fitting and impedance spectra obtained from a series of measurements conducted on STO thin films on Nb:STO, utilizing microelectrodes of three sizes and at various temperatures. The impedance spectra contain two or three overlapping semicircles. In principle, this might be caused by the bulk conduction of the STO and one or two space charge regions at the contacts. However, in a previous work on PLD-deposited STO films similar spectra were obtained, and a different interpretation was made: The different semicircles are caused by a transition from pure electron conduction at low frequency (R_{DC}) to the total conductivity (also including oxide ion conduction) at higher frequencies. Actually, this type of impedance response would require a fit with transmission line [54], but in our study we mainly aimed at the R_{DC} value. Therefore, a simpler fit using 3 serial R-CPE elements were made, and a fit example is shown in Figure 4.22. Additionally, Figure 4.22a exhibits the circuits model for fitting the data, that was employed across the series of measurements on STO thin films on Nb:STO, including varying microelectrodes sizes and temperatures.

The magnification of the impedance spectra illustrated in Figure 4.22b better reveals the shoulder at high frequencies, around 31 kHz. For a first approximation, the high frequency arc is attributed to the total (ionic and electronic) conductivity of STO. This interpretation is supported by the measured capacitance, wherein the high-frequency shoulder of the impedance spectrum exhibits a capacitance approximately ten times less than that of the other two regions, indicating geometric capacitance effects for the shoulder at high frequency.

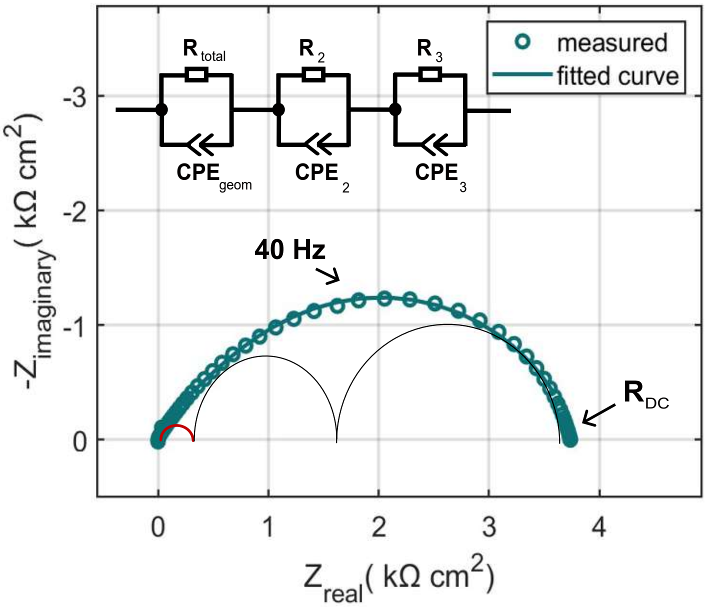

(a) Impedance spectra of STO film with the high frequency arc shown in red

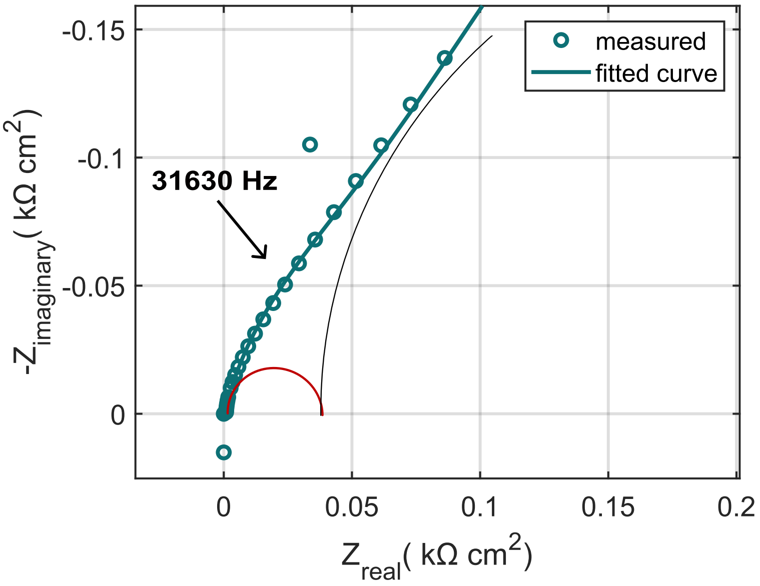

(b) The magnification of the impedance spectra with a high-frequency shoulder, attributed to the total conductivity of the STO thin film

Figure 4.22: Impedance spectrum of an STO thin film on a Nb:STO single crystal substrate (shown in red) measured with a 692 μm radius microelectrode at 500 °C

The total conductivity of the STO thin film on Nb:STO was calculated using Equation (4.6):

$$\sigma = \frac{1}{R_{STO}} \times \frac{d}{A} \tag{4.6}$$

where A represents the area of the microelectrode used for the measurement, and d denotes the thickness of the STO thin film, as determined from the SEM image shown in Figure 4.23.

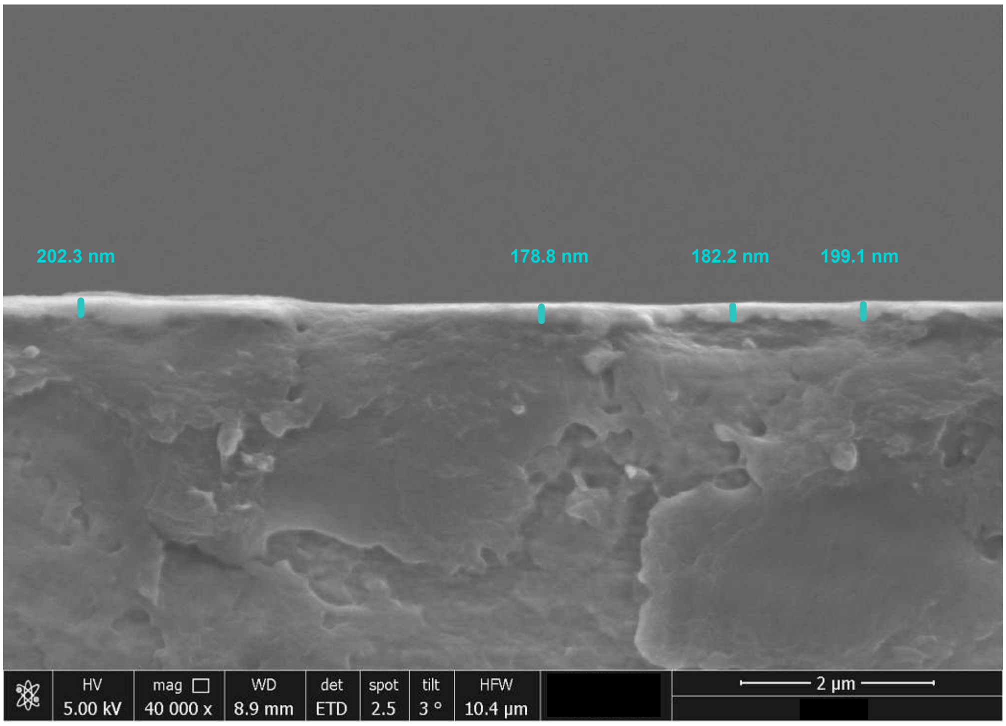

Figure 4.23: Cross-section SEM image of the STO thin film on Nb:STO, where the thickness is approximately 200 nm

Figure 4.24 shows the total conductivity of the STO thin film grown on Nb:STO measured with microelectrodes sized 692 µm, 549 µm, and 413 µm within a temperature range of 500 to 600 °C. By raising the temperature, the conductivity of the STO thin film increases.

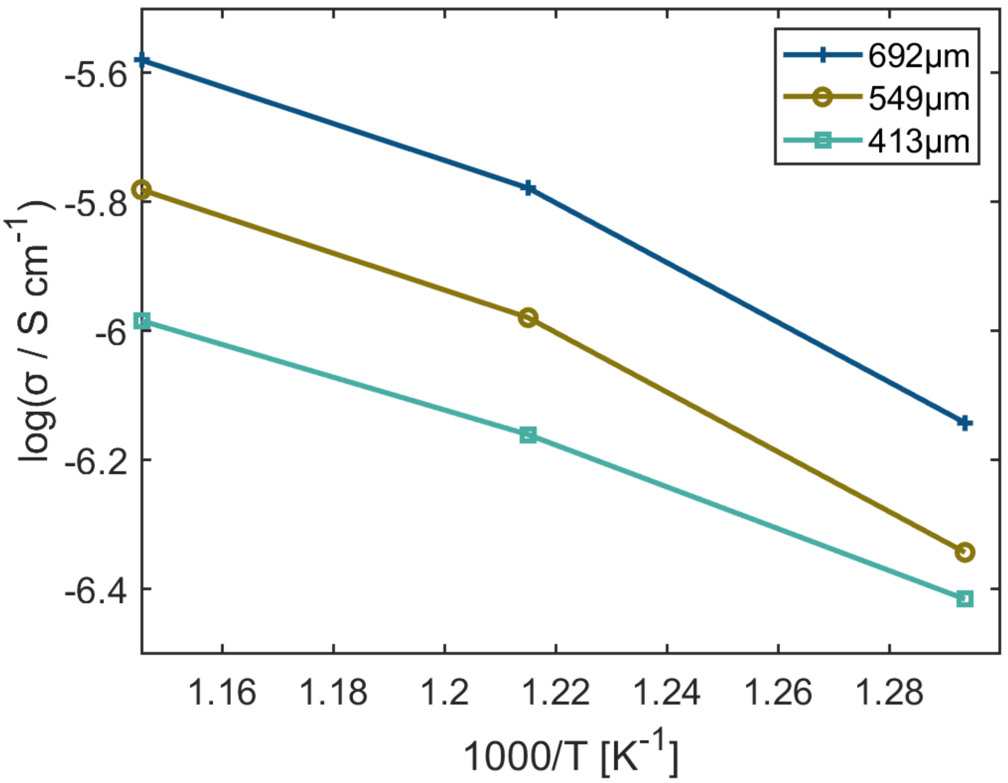

Figure 4.24: The total conductivity of the STO thin film grown on Nb:STO, from impedance spectra measured with microelectrodes sizes varied 692 µm, 549 µm, and 413 µm within a temperature range of 500 °C to 600 °C. The total conductivity has calculated from R_{STO} found in the high-frequency shoulder in the impedance spectra.

Figure 4.25 illustrates the conductivity calculated (as mentioned in previous section Equation (4.6)) from the DC resistance extracted from the impedance measurements conducted with microelectrodes sized 692 µm, 549 µm, and 413 µm, with a temperature range of 500 to 600 °C. The electronic conductivity of the STO thin film is notably ultra low. However, it is very close to the so called persudo-intrinsic conductivity of the STO thin film prepared by PLD-deposition [54]. Even the activation energies of ca 1.7-1.8 eV fits well with the value of the literatures on persudo-intrinsic films. This is approximately half the band gap energy and is caused by a pining of the Fermi-level mid-gap by Sr vacancy.

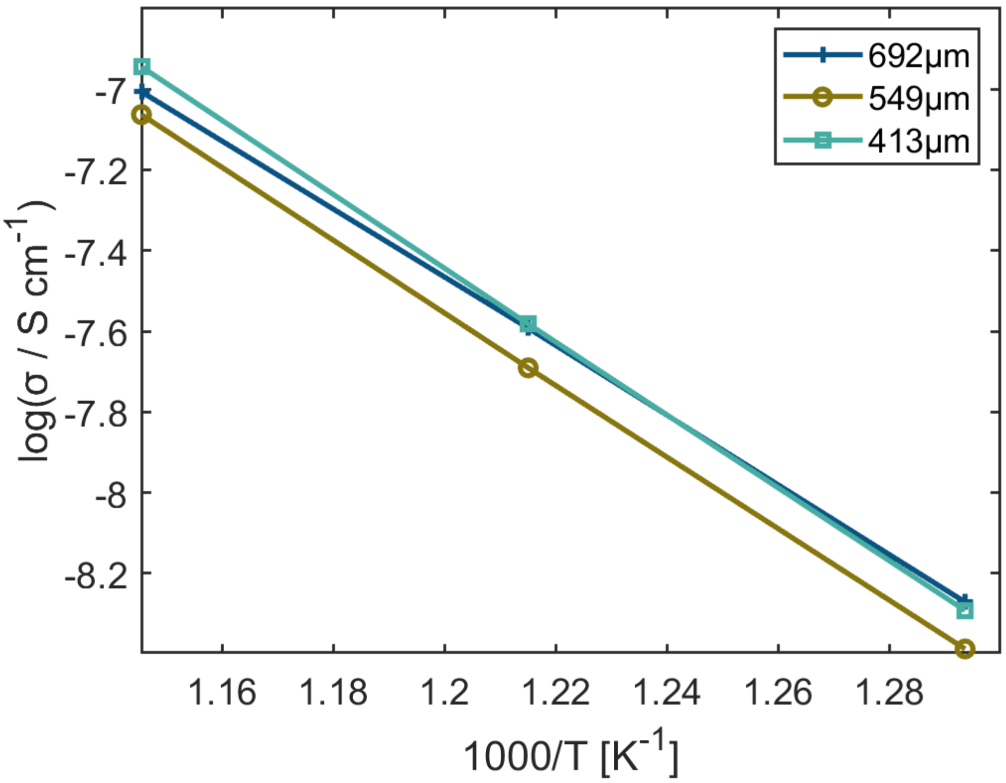

FIGURE 4.25: The electronic conductivities of the STO thin film grown on Nb:STO were determined by extracting R_{DC} from the impedance spectra obtained through impedance spectroscopy. Measurements were conducted using microelectrodes 692 µm, 549 µm, and 413 µm, covering a temperature range of 500 °C to 600 °C.

4.2.3 Half cell battery

Titanium exhibits comparatively low reducibility, when compared to other materials such as cobalt, or iron in the electrochemical series, primarily due to its lower standard electrochemical potential. This characteristic makes STO a promising material for use as an anode in oxygen-ion batteries. The STO thin film in half cell battery work as an anode and LSF work a cathode, due to the lower affinity of titanium becoming to reduce in the STO thin film compared to the iron present in LSF. By applying a positive current (getting electron from counter collector e_{cc}^{-}), the STO thin film undergoes reduction, resulting in the creation of one oxygen vacancy per two electrons inside STO thin film (oxygen removal). The removed oxygen ion can then conduct through the electrolyte, in this case YSZ, to reach the cathode (LSF). Equation (4.7) shows the oxygen exchange reaction in the Kröger-Vink-Notation [8].

$$O_o^x + 2e_{cc}^- + 2h^\bullet \rightleftharpoons V_o^{\bullet\bullet} + O_{YSZ}^{2-} \tag{4.7}$$

Ten cycles of oxygen removal and oxygen insertion were conducted on a STO thin film. Each cycle involved the removal of oxygen from the STO thin film by applying a current of 20 µA until reaching a lower cutoff voltage. Subsequently, a current of -20 µA was applied to insert oxygen into the STO thin film. This cyclic process aims to demonstrate the potential for reversible chemical reactions within the STO thin film, in accordance with the process observed in a full oxygen-ion battery.

A lower cutoff voltage of -2.08 V (vs. 1 bar O_2) was established to prevent too much oxygen removal from the STO material, which could lead to irreversible reactions or structural damage. This voltage was selected based on previous measurements of STO thin films on YSZ, which revealed the highest chemical capacity at lower voltages vs. Fe/FeO. This finding confirms the presence of a higher concentration of oxygen vacancies at lower voltages without irreversibly damaging the STO perovskite structure. Figure 4.26 shows the ten cycles wherein a current of 20 µA was applied to achieve the lower cut-off voltage of -2.08 V vs. 1 bar O_2. The first cycle is excluded from further analysis due to showing different behavior that might be related to the history of the STO thin film or irreversible process that might be taking place in the first cycle.

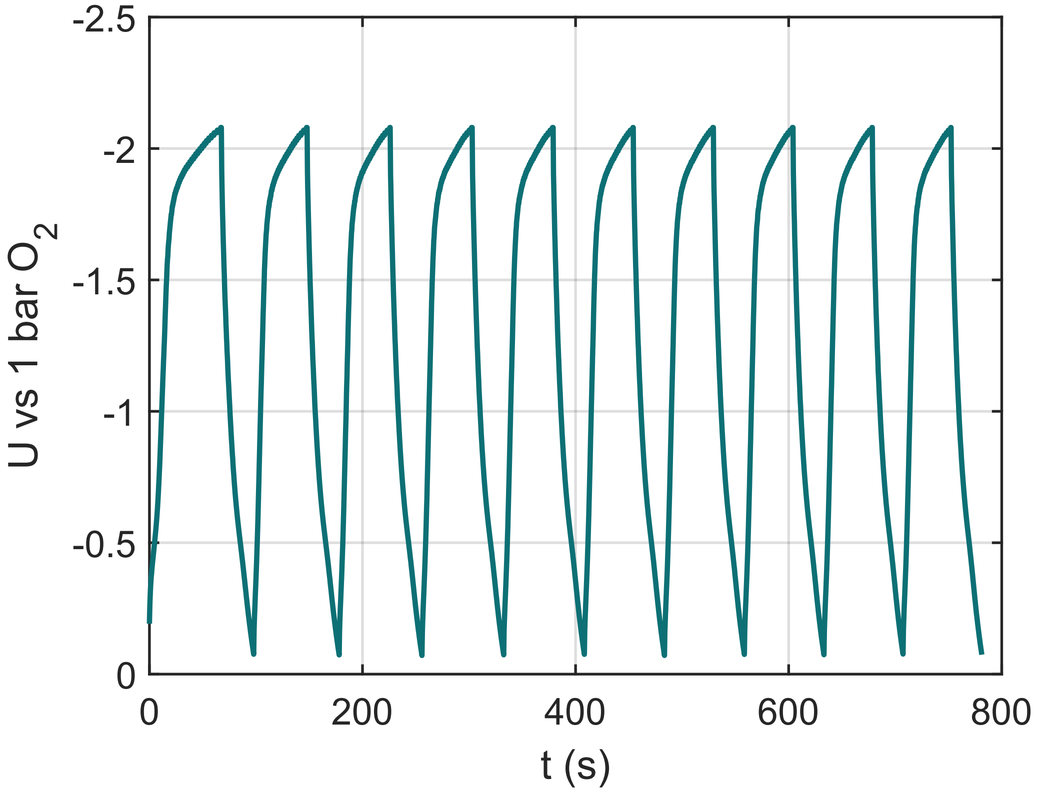

Figure 4.26: Galvanostatic measurement of an STO thin film anode on YSZ, cycled with ± 20 µA current to a lower cut-off voltage of -2.08V vs. 1 bar O_2 at 500 °C

Figure 4.27 provides a detailed view of one measured cycle out of the ten measured cycles, illustrating the oxygen removal from the STO thin film by applying 20 µA, followed by reaching the lower cut-off voltage and then applying -20 µA to insert the oxygen back into the STO thin film.

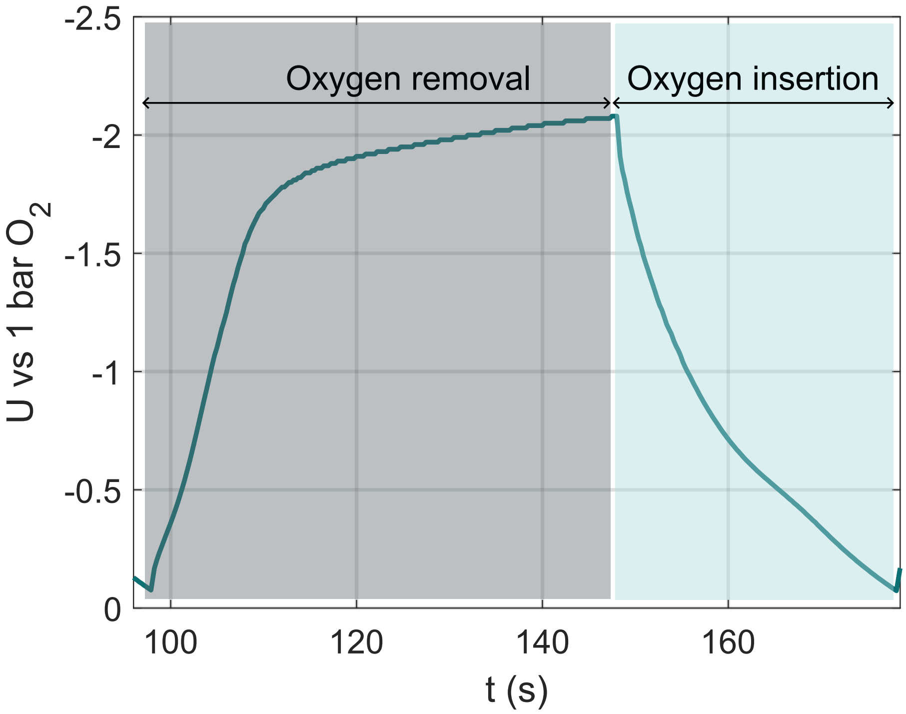

FIGURE 4.27: Detailed illustration of a measured cycle of an STO anode with an applied current of ± 20 µA and a lower cut-off voltage of -2.08 vs. 1 bar O_2 at 500 °C

In each cycle, it is evident that the removal of oxygen takes longer than oxygen insertion. This asymmetry may be attributed to the glass layer on top, which does not effectively prevent oxygen uptake from the atmosphere, resulting in what could be referred to as a leak current. To estimate the magnitude of the leak current, currents of 7, 8, 9, and 10 µA were applied to the STO thin film, with a lower cutoff voltage of -1.9 V vs. 1 bar. Figure 4.28 illustrates the applied cycles over time.

When applying a current of 7 µA (Figure 4.28 a), it was observed that the lower cutoff voltage could not be reached, indicating that the maximal leakage current in the used voltage range is higher than 7 µA. This suggests that an oxygen leakage, probably through the glass layer, is causing oxygen insertion into the STO, which can oxidize the STO thin film, rather than reducing it. Gradually increasing the applied current resulted in eventually reaching the lower cutoff voltage at current higher than 7 µA.

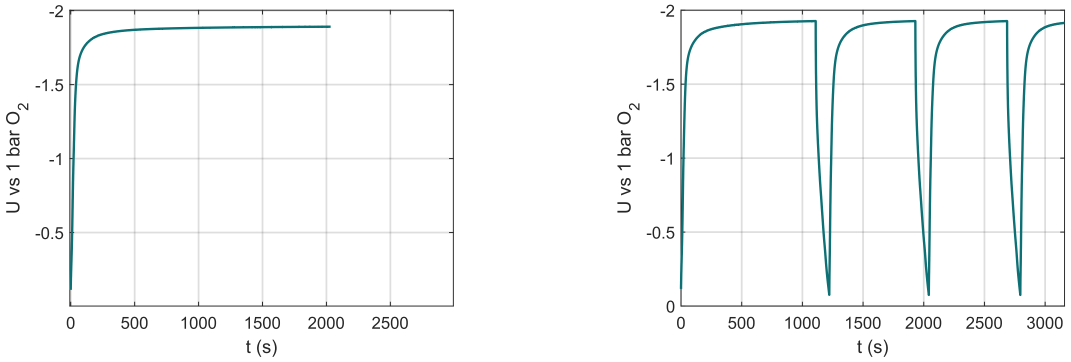

(a) Current of 7 µA with a lower cut-off voltage of -1.9 V vs. 1 bar O_2

(b) Current of 8 µA with a lower cut-off voltage of -1.9 V vs. 1 bar O_2

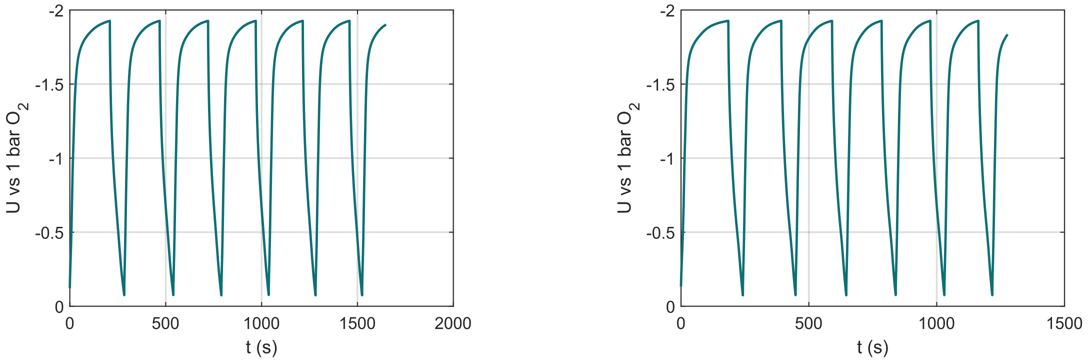

(c) Current of 9 µA with a lower cut-off voltage of -1.9 V vs. 1 bar O_2

(d) Current of 10 µA with a lower cut-off voltage of -1.9 V vs. 1 bar O_2

FIGURE 4.28: Galvanostatic cycling of the STO anode with a cut-off voltage of -1.9 V vs. 1 bar O_2 and a current of a) 7 µA, b) 8 µA, c) 9 µA and d) 10 µA, to assess the leak current, that arises due to improper sealing of the STO thin film with glass.

To demonstrate the feasibility of employing STO as a battery material, we calculated the volumetric charge of STO thin films from the cyclic galvanostatic measurement (previously shown in Figure 4.26). Calculation of the volumetric charge involved integrating the measured current and subsequently normalizing it to the total volume of the thin film electrode. The volumetric charge, quantified in units of milliampere-hour per cubic centimeter (mAh/cm^3), represents the electric charge stored per unit volume of a material.

To calculate the volume of the STO thin film, an SEM image was taken from the cross-section of a STO thin film on the YSZ. Figure 4.29 shows the thickness of the film on YSZ. The area of the STO electrode was measured with a light microscope (previously shown in Figure 3.6).

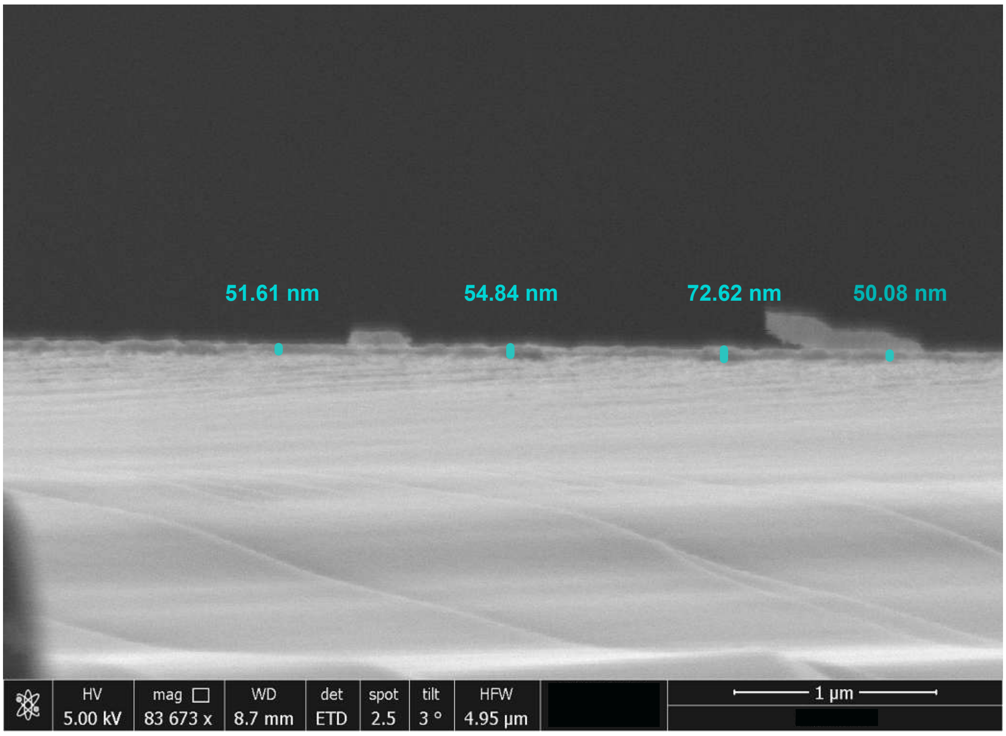

FIGURE 4.29: Cross-section SEM image of a STO thin film on a YSZ single crystal, where the thickness of the film is approximately 50 nm

As demonstrated in Figure 4.30, the volumetric charge was calculated for each galvanostatic cycle, involving both the removal and insertion of oxygen.

The volumetric charge associated with the removal of oxygen from the STO thin film should ideally match the volumetric charge required for its insertion back into the film. However, deviations between charge and discharge rates may arise, potentially attributed to oxygen leakage from the surrounding atmosphere.

The coulomb efficiency(CE) of the STO thin film was calculated through:

$$CE = \frac{t_{\text{oxygen removal}}}{t_{\text{oxygen insertion}}} \tag{4.8}$$

where $t_{\text{oxygen removal}}$ represents the duration of oxygen removal for each cycle (in seconds), and $t_{\text{oxygen insertion}}$ denotes the duration of oxygen insertion for each cycle (also in seconds). In this measurement, a nearly constant current was applied, hence the coulomb efficiency was determined without the need for time integration. The investigated sol-gel STO thin film exhibited an efficiency of approximately 60%. Figure 4.30b despite the coulomb efficiency of each cycle. Future enhancement of the STO thin film's efficiency might be achieved through modifications to the sealing process to minimize oxygen leakage into the cell [8].

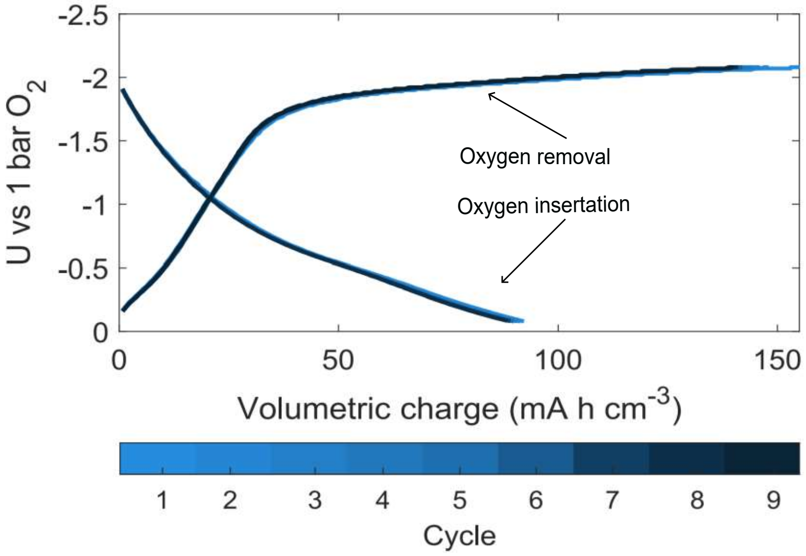

(a) Volumetric charge of the STO thin film measured in a half-cell at 500 °C. The measurements were obtained by applying a ± 20 μA current and utilizing a cut-off voltage of -2.08 V vs. 1 bar O_2 over 9 cycles

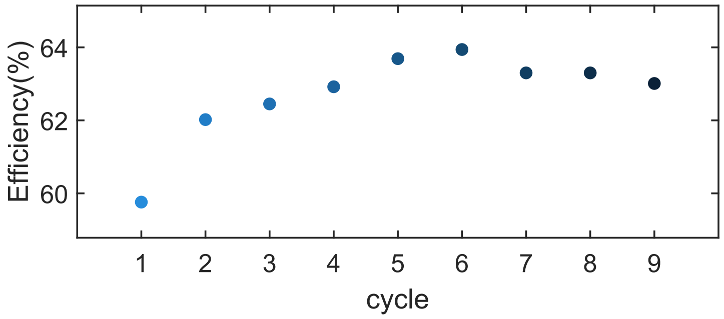

(b) Coulomb efficiency of each cycle

FIGURE 4.30: Volumetric charge and coulomb efficiency of the STO thin film in a half cell battery

5 Summary and outcome

STO precursors were synthesized via the sol-gel process. Subsequently, thin films were spin-coated onto YSZ single crystals, followed by heat treatment and annealed to crystallization of the perovskite structure. Analytical characterization was performed using GIXRD, EIS, and LA-ICP-MS methods.

The characterization of STO thin films aimed to achieve four main objectives and yielded the following results:

- Investigation into the effect of annealing temperature on STO thin films prepared via the sol-gel method revealed crystallization occurring at temperatures above 550 °C.
- Assessment of the impact of STO precursor aging demonstrated the stability of the perovskite structure over time. Additionally, SEM images exhibited almost consistent surface morphologies.
- Examination of the Sr:Ti ratio variation in the precursor revealed that a Sr depletion results consistently regardless of the Sr:Ti ratio. GIXRD analysis showed an amorphous structure for the 0.5:1 Sr:Ti ratio, while the 2:1 ratio exhibited a Ruddlesden-Popper-type perovskite structure, which is of interest for conductivity measurements.
- Evaluation of the reproducibility of the sol-gel method in producing STO thin films confirmed successful outcomes using analytical techniques except the surface morphologies.

Three approaches were employed for the electrochemical characterization of the STO thin films grown on YSZ and Nb:STO, prepared via the sol-gel process. These approaches included the calculation of the oxygen vacancy concentration from the chemical capacitance, the electronic conductivity of STO thin films, and validation of the concept that the STO thin films can be utilized as an oxygen ion batteries. The outcomes of these measurements can be summarized as follows:

- Impedance measurements of STO sol-gel thin film under applied bias voltage, employing an innovative approach involving the use of GDC/FeO for controlling oxygen nonstoichiometry, enabled us to regulate oxygen activity within the range of 10^{-3} to 10^{-55} bar. The findings revealed an approximate concentration of 10^{18} cm^{-3} of oxygen vacancies at very lower oxygen activities. Remarkably, these results were in close agreement with the oxygen vacancy concentrations calculated from the Brouwer diagram at almost the same partial pressure and temperature for 6 ppm Ti vacancies.

- STO thin film on Nb:STO for conductivity measurements, exhibited an ultra-low electronic conductivity characteristic consistent with previous measurements. The values are close to those of STO with mid-gap Fermi energy (i.e. persudo intrinsic)

- STO thin film as an electrode in a half cell battery were spin-coated with the desired shape on YSZ with a LSF counter electrode. Charging experiments successfully proved that this material has the potential to be used as an electrode in an oxygen ion battery. The remarkable voltage of -2.08 V vs. 1 bar O_2 was achieved, although the coulomb efficiency of this electrode material was still mediocre. The reason could be the glass sealing, which still does not completely block an oxygen uptake from the atmosphere. This can be approved by future measurements with a different sealing material.

6 Acknowledgement

The road of my master studies is nearing its end. I would like to express my deepest appreciation to my professor Jürgen Fleig, who gave me this wonderful opportunity to work on a super interesting topic with a great team. I am extremely grateful to have Claudia Steinbach as a supervisor, who helped me to reach my best. I could not undertake this journey without you and your patience towards my questions.

Words cannot express my gratitude for my lovely parents, who not only financially but also emotionally always supported me, regardless of my decisions in my life. You guys gave me the power and strength to overcome the problems and never give up.

My beloved person David came through this roller coaster with me, heard my words with his beautiful heart every day, gave me endless love and support. I am extremely grateful to have you by my side.

My best friend Shirin, who gave me encouragement from a long way from Tehran supported me and listened to all of my words, I am extremely grateful for your support.

I had the pleasure to be in the greatest office in the institute, which was shared with Meli, Milena, Stani, and Glix. Stani your zwetschkenknödels are the best and gave me the energy to even work more. Glix “man migam mercy”, you brought a wonderful energy with your presence in our office. Meli it was a great time with you in the office. Milena you came later to our office, but your presence was great.

At the end I want to thank all of our group who are great, helpful, and the best. I am also thankful for the opportunity that I had for studying in beautiful Vienna city.

Acronyms

AFM Atomic Force Microscopy. 23, 44, 54

EIS Electrochemical Impedance Spectroscopy. ii, 14, 31, 32, 35, 56, 64, 77

GDC Gd:CeO_2. 24, 32

GIXRD Grazing Incidence X-Ray Diffraction. ii, 23, 30, 38, 39, 41, 43, 48–51, 77

LA-ICP-MS Laser Ablation Inductively Coupled Plasma Mass Spectrometry. ii, 23, 30, 42, 43, 47, 50, 51, 77

LSF $La_{0.6}Sr_{0.4}FeO_{3-\delta}$. 27, 28, 78

MIEC Mixed Ion Electron Conductors. 1, 2

Nb:STO Nb-doped $SrTiO_3$. ii, iii, 25, 35, 56, 64–66, 68, 77, 78

SEM Scanning Electron Microscope. 23, 30, 41, 44, 49, 50, 52, 54, 62, 74, 77

YSZ Yttria-stabilized zirconia. ii, iii, 22–24, 27–29, 38, 42, 44, 47, 48, 50–57, 59, 71, 74, 77, 78

List of Figures

List of Tables

Bibliography

[1] S. W. Lee, O. S. Kwon, J. H. Han, and C. S. Hwang. “Enhanced electrical properties of SrTiO3 thin films grown by atomic layer deposition at high temperature for dynamic random access memory applications”. In: *Applied physics letters* 92.22 (2008).

[2] L. Enzlberger. “Photovoltaic properties of SrTiO3-δ in single crystalline and thin film cells”. TU Wien, 2022.

[3] M. Morgenbesser, A. Schmid, A. Viernstein, J. de Dios Sirvent, F. Chiabrera, N. Bodenmüller, S. Taibl, M. Kubicek, F. Baiutti, A. Tarancon, and J. Fleig. “SrTiO3 based high temperature solid oxide solar cells: Photovoltages, photocurrents and mechanistic insight”. In: *Solid State Ionics* 368 (2021), p. 115700.

[4] S. Wang, A. Kawase, and H. Ogawa. “Preparation and Characterization of Multilayer Capacitor with SrTiO3 Thin Films by Aerosol Chemical Vapor Deposition”. In: *Japanese Journal of Applied Physics* 45.9S (Sept. 2006), p. 7252.

[5] J. Liu, Y. Wang, X. Zhai, Y. Xue, L. Hao, H. Zhu, C. Liu, H. Cheng, and J. Ouyang. “Energy Storage Properties of Sol–Gel-Processed SrTiO3 Films”. In: *Materials* 16.1 (2022), p. 31.

[6] D. Bao, H. Yang, L. Zhang, and X. Yao. “Structure and optical properties of SrTiO3 thin films prepared by a sol–gel technique”. In: *physica status solidi (a)* 169.2 (1998), pp. 227–233.

[7] O. Okhay, A. Tkach, A. Wu, and P. Vilarinho. “Manipulation of dielectric permittivity of sol–gel SrTiO3 films by deposition conditions”. In: *Journal of Physics D: Applied Physics* 46.50 (2013), p. 505315.

[8] A. Schmid, M. Krammer, and J. Fleig. “Rechargeable Oxide Ion Batteries Based on Mixed Conducting Oxide Electrodes”. In: *Advanced Energy Materials* 13.11 (2023), p. 2203789.

[9] B. Wagner. “Investigating mixed conducting oxygen storage electrodes via chemical capacitance measurements”. TU Wien, 2023.

[10] M. Pitteri and G. Zanzotto. “On the definition and classification of Bravais lattices”. In: *Acta Crystallographica Section A: Foundations of Crystallography* 52.6 (1996), pp. 830–838.

[11] E. McCalla, J. Walter, and C. Leighton. “A unified view of the substitution-dependent antiferrodistortive phase transition in SrTiO3”. In: *Chemistry of Materials* 28.21 (2016), pp. 7973–7981.

[12] A. G. H. Smith. “Structural and defect properties of strontium titanate”. PhD thesis. UCL (University College London), 2012.

[13] C. Xie, D. Yan, H. Li, S. Du, W. Chen, Y. Wang, Y. Zou, R. Chen, and S. Wang. “Defect chemistry in heterogeneous catalysis: recognition, understanding, and utilization”. In: *ACS Catalysis* 10.19 (2020), pp. 11082–11098.

[14] R. J. Tilley. *"Defects in solids"*. John Wiley & Sons, 2008.

[15] S.-J. L. Kang. “12 - SINTERING ADDITIVES AND DEFECT CHEMISTRY”. In: *Sintering*. Ed. by S.-J. L. Kang. Oxford: Butterworth-Heinemann, 2005, pp. 173–179. ISBN: 978-0-7506-6385-4.

[16] F. Kröger and H. Vink. “Relations between the Concentrations of Imperfections in Crystalline Solids”. In: ed. by F. Seitz and D. Turnbull. Vol. 3. Solid State Physics. Academic Press, 1956, pp. 307–435.

[17] A. Thakre and A. Kumar. “Unipolar resistive switching in sol-gel synthesized strontium titanate thin films”. In: *Vacuum* 151 (May 2018), pp. 182–184.

[18] E. Ellmeyer. “Oxygen nonstoichiometry in undoped and iron-doped strontium titanate”. TU Wien, 2020.

[19] J.-L. Zhang and G.-Y. Hong. “Nonstoichiometric compounds”. In: *Modern inorganic synthetic chemistry*. Elsevier, 2017, pp. 329–354.

[20] C. B. Carter and M. G. Norton. “Point defects, charge, and diffusion”. In: *Ceramic Materials: Science and Engineering* (2007), pp. 181–200.

[21] T.-T. Fang. *"Elements of structures and defects of crystalline materials"*. Elsevier, 2018.

[22] V. B. Tinti, A. Kabir, D. Zanetti de Florio, and V. Esposito. “11 - The role of dopant on the defect chemistry of metal oxides”. In: *Metal Oxide Defects*. Ed. by V. Kumar, S. Som, V. Sharma, and H. C. Swart. Metal Oxides. Elsevier, 2023, pp. 313–353.

[23] M. J. Akhtar, Z.-U.-N. Akhtar, R. A. Jackson, and C. R. A. Catlow. “Computer simulation studies of strontium titanate”. In: *Journal of the American Ceramic Society* 78.2 (1995), pp. 421–428.

[24] D. M. Morgenbesser. “Nonstoichiometry in SrTiO3 and its relevance for tunable conductivity and photovoltage”. PhD thesis. TU Wien, 2021.

[25] R. A. De Souza, J. Fleig, R. Merkle, and J. Maier. “SrTiO3: a model electroceramic”. In: *International Journal of Materials Research* 94.3 (2022), pp. 218–225.

[26] R. De Souza. “Oxygen diffusion in SrTiO3 and related perovskite oxides”. In: *Advanced Functional Materials* 25.40 (2015), pp. 6326–6342.

[27] I. Denk, W. Münch, and J. Maier. “Partial conductivities in SrTiO3: bulk polarization experiments, oxygen concentration cell measurements, and defect-chemical modeling”. In: *Journal of the American Ceramic Society* 78.12 (1995), pp. 3265–3272.

[28] J. Maier. “Defect chemistry: composition, transport, and reactions in the solid state; part I: thermodynamics”. In: *Angewandte Chemie International Edition in English* 32.3 (1993), pp. 313–335.

[29] M. Siebenhofer. “Investigating point defect concentrations and their impact on surface exchange reaction rates of mixed ionic and electronic conductors”. PhD thesis. TU Wien, 2021.

[30] R. Merkle and J. Maier. “How is oxygen incorporated into oxides? A comprehensive kinetic study of a simple solid-state reaction with SrTiO3 as a model material”. In: *Angewandte Chemie International Edition* 47.21 (2008), pp. 3874–3894.

[31] M. Guglielmi. “Sol-gel coatings on metals”. In: *Journal of sol-gel science and technology* 8 (1997), pp. 443–449.

[32] S. Tian, Z. Liu, L. Shen, J. Pu, W. Liu, X. Sun, and Z. Li. “Performance evaluation of mercapto functional hybrid silica sol–gel coating and its synergistic effect with f-GNs for corrosion protection of copper surface”. In: *RSC advances* 8.14 (2018), pp. 7438–7449.

[33] N. Shanmugam, R. Pugazhendhi, R. Madurai Elavarasan, P. Kasiviswanathan, and N. Das. “Anti-reflective coating materials: A holistic review from PV perspective”. In: *Energies* 13.10 (2020), p. 2631.

[34] R. Vijayalakshmi and V. Rajendran. “Synthesis and characterization of nano-TiO2 via different methods”. In: *Arch. Appl. Sci. Res* 4.2 (2012), pp. 1183–1190.

[35] A. Jaroenworaluck, W. Sunsaneeyametha, N. Kosachan, and R. Stevens. “Characteristics of silica-coated TiO2 and its UV absorption for sunscreen cosmetic applications”. In: *Surface and Interface Analysis: An International Journal devoted to the development and application of techniques for the analysis of surfaces, interfaces and thin films* 38.4 (2006), pp. 473–477.

[36] C. D. Lakeman and D. A. Payne. “Sol-gel processing of electrical and magnetic ceramics”. In: *Materials Chemistry and Physics* 38.4 (1994), pp. 305–324.

[37] L. L. Hench and J. K. West. “The sol-gel process”. In: *Chemical reviews* 90.1 (1990), pp. 33–72.

[38] A. C. Pierre. *"Introduction to sol-gel processing"*. Springer Nature, 2020.

[39] M. Parashar, V. K. Shukla, and R. Singh. “Metal oxides nanoparticles via sol–gel method: a review on synthesis, characterization and applications”. In: *Journal of Materials Science: Materials in Electronics* 31 (2020), pp. 3729–3749.

[40] D. Navas, S. Fuentes, A. Castro-Alvarez, and E. Chavez-Angel. “Review on sol-gel synthesis of perovskite and oxide nanomaterials”. In: *Gels* 7.4 (2021), p. 275.

[41] H. S. Magar, R. Y. Hassan, and A. Mulchandani. “Electrochemical impedance spectroscopy (EIS): Principles, construction, and biosensing applications”. In: *Sensors* 21.19 (2021), p. 6578.

[42] H. H. Hernández, A. R. Reynoso, J. T. González, C. G. Morán, J. M. Hernández, A. M. Ruiz, J. M. Hernández, and R. O. Cruz. “Electrochemical impedance spectroscopy (EIS): A review study of basic aspects of the corrosion mechanism applied to steels”. In: *Electrochemical Impedance Spectroscopy* (2020), pp. 137–144.

[43] P. Vadhva, J. Hu, M. J. Johnson, R. Stocker, M. Braglia, D. J. Brett, and A. J. Rettie. “Electrochemical impedance spectroscopy for all-solid-state batteries: Theory, methods and future outlook”. In: *ChemElectroChem* 8.11 (2021), pp. 1930–1947.

[44] A. C. Lazanas and M. I. Prodromidis. “Electrochemical impedance spectroscopy a tutorial”. In: *ACS Measurement Science Au* 3.3 (2023), pp. 162–193.

[45] S. Breitwieser. “Oxygen stoichiometry of A-site-deficient perovskites for solid oxide cells”. Wien, 2023.

[46] R. D. Holmes, H. S. O’Neill, and R. J. Arculus. “Standard Gibbs free energy of formation for Cu2O, NiO, CoO, and FexO: High resolution electrochemical measurements using zirconia solid electrolytes from 900–1400 K”. In: *Geochimica et Cosmochimica Acta* 50.11 (1986), pp. 2439–2452. ISSN: 0016-7037.

[47] M. Siebenhofer, A. Nenning, C. Rameshan, P. Blaha, J. Fleig, and M. Kubicek. “Engineering surface dipoles on mixed conducting oxides with ultra-thin oxide decoration layers”. In: *Nature Communications* 15.1 (2024), p. 1730.

[48] A. Nenning and J. Fleig. “Electrochemical XPS investigation of metal exsolution on SOFC electrodes: Controlling the electrode oxygen partial pressure in ultra-high-vacuum”. In: *Surface Science* 680 (2019), pp. 43–51.

[49] A. F. Wells. *"Structural inorganic chemistry"*. Oxford University Press, USA, 2012.

[50] C. Xu, H. Du, A. J. van der Torren, J. Aarts, C.-L. Jia, and R. Dittmann. “Formation mechanism of Ruddlesden-Popper-type antiphase boundaries during the kinetically limited growth of Sr rich SrTiO3 thin films”. In: *Scientific reports* 6.1 (2016), p. 38296.

[51] J.-H. Park and R. N. Blumenthal. “Electronic Transport in 8 Mole Percent Y 2 O 3-ZrO2”. In: *Journal of the Electrochemical Society* 136.10 (1989), p. 2867.

[52] M. Krammer, A. Schmid, M. Kubicek, and J. Fleig. “Utilizing oxygen gas storage in rechargeable oxygen ion batteries”. In: *Journal of Power Sources* 577 (2023), p. 233167.

[53] J. Fleig, G. M. Rupp, A. Nenning, and A. Schmid. “(Invited) Towards an Improved Understanding of Electrochemical Oxygen Exchange Reactions on Mixed Conducting Oxides”. In: *ECS Transactions* 77.10 (May 2017), p. 93.

[54] M. Morgenbesser, S. Taibl, M. Kubicek, A. Schmid, A. Viernstein, N. Bodenmüller, C. Herzig, F. Baiutti, J. de Dios Sirvent, M. O. Liedke, et al. “Cation non-stoichiometry in Fe: $SrTiO_3$thin films and its effect on the electrical conductivity”. In: *Nanoscale Advances* 3.21 (2021), pp. 6114–6127.